



Micromechanical constitutive model for low-temperature constant strain rate deformation of limestones in the brittle and semi-brittle regime

A Nicolas, J Fortin, Y Guéguen

► To cite this version:

A Nicolas, J Fortin, Y Guéguen. Micromechanical constitutive model for low-temperature constant strain rate deformation of limestones in the brittle and semi-brittle regime. *Geophysical Journal International*, 2017, 211 (1), pp.300 - 321. 10.1093/gji/ggx299 . hal-03978427

HAL Id: hal-03978427

<https://cnrs.hal.science/hal-03978427>

Submitted on 8 Feb 2023

HAL is a multi-disciplinary open access archive for the deposit and dissemination of scientific research documents, whether they are published or not. The documents may come from teaching and research institutions in France or abroad, or from public or private research centers.

L'archive ouverte pluridisciplinaire **HAL**, est destinée au dépôt et à la diffusion de documents scientifiques de niveau recherche, publiés ou non, émanant des établissements d'enseignement et de recherche français ou étrangers, des laboratoires publics ou privés.

Micromechanical constitutive model for low-temperature constant strain rate deformation of limestones in the brittle and semi-brittle regime

A. Nicolas, J. Fortin and Y. Guéguen

Laboratoire de Géologie, Ecole Normale Supérieure - PSL Research University -, CNRS, UMR 8538, Paris, France. E-mail: aurelien.nicolas89@gmail.com

Accepted 2017 July 13. Received 2017 July 12; in original form 2016 October 14

SUMMARY

Deformation and failure of rocks are important for a better understanding of many crustal geological phenomena such as faulting and compaction. In carbonate rocks among others, low-temperature deformation can either occur with dilatancy or compaction, having implications for porosity changes, failure and petrophysical properties. Hence, a thorough understanding of all the micromechanisms responsible for deformation is of great interest. In this study, a constitutive model for the low-temperature deformation of low-porosity (<20 per cent) carbonate rocks is derived from the micromechanisms identified in previous studies. The micromechanical model is based on (1) brittle crack propagation, (2) a plasticity law (interpreted in terms of dislocation glide without possibility to climb) for porous media with hardening and (3) crack nucleation due to dislocation pile-ups. The model predicts stress–strain relations and the evolution of damage during deformation. The model adequately predicts brittle behaviour at low confining pressures, which switches to a semi-brittle behaviour characterized by inelastic compaction followed by dilatancy at higher confining pressures. Model predictions are compared to experimental results from previous studies and are found to be in close agreement with experimental results. This suggests that microphysical phenomena responsible for the deformation are sufficiently well captured by the model although twinning, recovery and cataclasis are not considered. The porosity range of applicability and limits of the model are discussed.

Key words: Defects; Elasticity and anelasticity; Fracture and flow; Plasticity, diffusion, and creep; Geomechanics; Microstructures.

1 INTRODUCTION

Understanding and predicting the mechanical behaviour of carbonate rocks is of great interest for industrial purposes, because they are crossed by faults zones (Armijo *et al.* 1992; Willemse *et al.* 1997; Mouslopoulou *et al.* 2014), constitute the basement under some volcanoes (Heap *et al.* 2013) and host thermal water resources (e.g. Goldscheider *et al.* 2010) among other examples of application. Experimental studies have been conducted on limestones (e.g. Heard 1960; Olsson 1974; Vincké *et al.* 1998; Baud *et al.* 2000; Vajdova *et al.* 2004, 2010; Brantut *et al.* 2014; Brantut 2015; Nicolas *et al.* 2016), marbles (e.g. Rutter 1974; Fredrich *et al.* 1989; Renner *et al.* 2002; Schubnel *et al.* 2006), chinks (e.g. Rhett & Farrell 1991; Risnes *et al.* 2005). Focusing on limestones, these studies have shown that depending on the confining pressure, samples can have a brittle or a ductile behaviour, even at low (room) temperature (Fig. 1). The brittle–ductile transition depends on grain size, porosity and pore size (e.g. Vajdova *et al.* 2004; Zhu *et al.* 2010; Wong & Baud 2012).

At low confining pressure, features are typical of the brittle regime: (i) samples undergo an elastic compaction until a point

denoted C' (e.g. Wong *et al.* 1997; Baud *et al.* 2000) beyond which dilatancy takes place (Fig. 1, inset A); (ii) the differential stress reaches a peak beyond which strain softening is occurring, which is typical of shear localization (Brace 1978); (iii) Observation of the samples after deformation in the post-peak regime indicates that the deformation was localized in a shear fault. Deformation at microscopic scale is accommodated by microcrack nucleation and/or propagation and eventually their coalescence.

At confining pressure higher than a threshold depending on the rock (e.g. Wong & Baud 2012), porous limestones exhibit (1) an elastic compaction and (2) an inelastic shear-enhanced compaction associated with strain hardening beyond a critical stress denoted C^* (e.g. Wong *et al.* 1997; Baud *et al.* 2000). Yet, inelastic compaction is transient and volumetric strain reverses from inelastic compaction to dilatancy (Fig. 1, inset B) beyond a critical stress denoted $C^{*'} (Baud et al. 2000). These features (i) involving macroscopically distributed, dilatant deformation by both crystal plasticity (dislocation creep, twinning) and microcracking (e.g. Fredrich et al. 1989); (ii) leading to strains lying in the range 3–5 per cent at failure and (iii) inducing a pressure-dependent strength; are typical of the semi-brittle (ductile) regime as defined by$

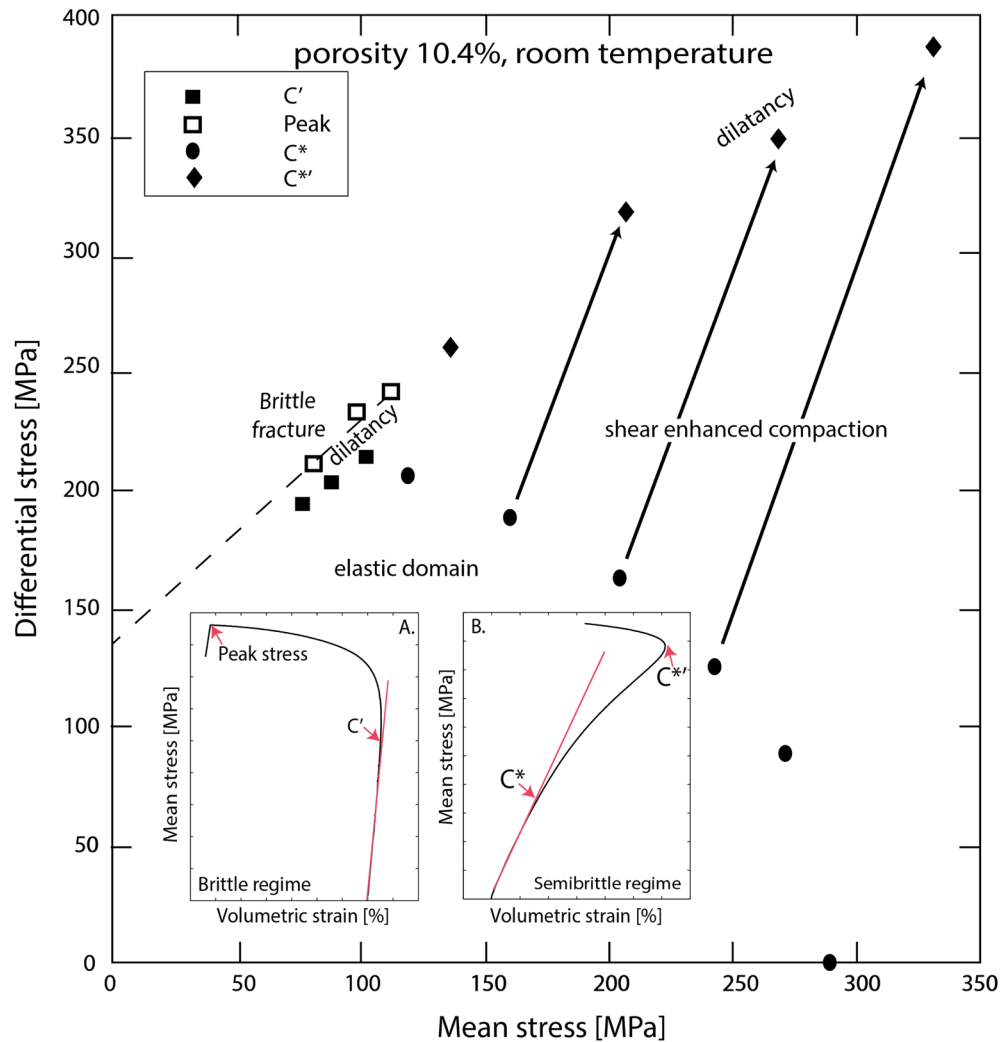


Figure 1. The failure envelope obtained by Vajdova *et al.* (2004) for Tavel limestone (porosity of 10.4 percent) deformed at constant strain rate under dry conditions at 20 °C. Inset A illustrates the evolution of mean stress as a function of volumetric strain for a constant strain rate experiment performed in the brittle regime. Inset B illustrates the evolution of mean stress as a function of volumetric strain for a constant strain rate experiment performed in the semi-brittle regime.

Evans *et al.* (1990), in agreement with Rutter (1986). The importance of this semi-brittle regime in the lithospheric deformation has been well recognized (e.g. Ross & Lewis 1989; Kohlstedt *et al.* 1995). At the microscale, microplasticity (mechanical twinning and dislocation glide) is active even at low temperature (Turner *et al.* 1954; Griggs *et al.* 1960; De Bresser & Spiers 1997). However, at low temperature, dislocations can only slip in their plane and twins cannot be eliminated, microdefects accumulate and no recovery process takes place. Localized residual stresses due to pile-ups can be sufficient to nucleate new microcracks (Smith & Barnby 1967; Evans *et al.* 1980; Wong 1990). Temperature plays a role (Rutter 1974) but only low temperature is considered in this article.

This study focuses on the development of a constitutive model for the prediction of the mechanical behaviour of limestones undergoing constant strain rate deformation at low temperature and various confining pressures. This model is micromechanically motivated: Assuming the micromechanisms considered previously, the aim is to predict the stress–strain relation. The model predictions are then compared to data available in the literature.

2 DEVELOPMENT OF THE CONSTITUTIVE MODEL

Limestones are heterogeneous in terms of microstructure (e.g. grain type and size, porosity distribution, cementation; see Lucia (2007) for details), thus physical properties and mechanical behaviour are not easy to predict (Anselmetti & Eberli 1993; Eberli *et al.* 2003; Baechle *et al.* 2008; Vajdova *et al.* 2012; Regnet *et al.* 2015a,b). For simplicity, in this model we assume that the microstructure is characterized by (1) a matrix composed of pure calcite, (2) a porosity made-up of equant pores and (3) cracks.

Predicting the mechanical behaviour of limestones implies to embody all the possible micromechanisms. Thus, the derivation of the micromechanically motivated constitutive model includes five key steps: (i) derive the effective elastic moduli for the cracked porous medium, (ii) calculate the macroscopic strains related to crack growth of an array of interacting cracks, (iii) calculate the macroscopic strains related to dislocations from crystal plasticity, (iv) account for crack nucleation and growth from dislocation pile-ups, and (v) finally calculate the macroscopic stress evolution during

Table 1. Summary of all the parameters used for the development of the model.

$\sigma, \sigma_m, \sigma_e$	Remotely applied stress tensor and corresponding mean and von-Mises effective stresses
Q, S	Remotely applied differential and deviatoric stresses
x	Stress triaxiality
ρ_c	Crack density as defined by Budiansky & O'Connell (1976)
G_i, G, K_i, K	Initial and current shear moduli, initial and current bulk moduli
G_0, G_u, K_0, K_u	Calcite and uncracked porous medium shear and bulk moduli
ν_0, ν_u, ν_i	Calcite, uncracked porous medium, and initial Poisson's ratios
K_I, K_{IC}	Stress intensity factor, and the critical value of the material
W	Strain energy density
$\varepsilon, \dot{\varepsilon}$	Remote strain and its rate of change
$\dot{\varepsilon}_{ax}$	Remotely imposed axial strain rate
$\dot{\varepsilon}^p$	Plastic strain rate
$\dot{\varepsilon}^d$	Strain rate induced by dislocations
$\varepsilon^{md}, \dot{\varepsilon}^{md}$	Strain induced by mobile dislocation motions and its rate of change
$\dot{\varepsilon}_0$	Reference strain rate for the non-porous material
ε_0	Yield strain for macroscopic plasticity
$\varepsilon^e, \varepsilon^{cracks}, \varepsilon^{mp}$	Strain due to elasticity, cracks, and plasticity of the porous material
ρ_d, ρ_{md}	Total and mobile dislocation densities
$\rho_{id}, \rho_{id}^{ini}, \rho_{id}^{new}$	Immobile dislocation density, decomposed as initial and newly nucleated
b	Burgers vector
v	Dislocation average slip velocity
V_0	Reference dislocation slip velocity
m, n	Stress sensitivity of the dislocation slip velocity and of the plasticity in the material
M	Strain hardening exponent of the macroscopic plastic law of the non-porous material
σ_0	Reference stress for dislocation slip velocity
σ_p, σ_p^i	Reference stress for plasticity of the non-porous material and its initial value
σ_i	Internal stress
$\sigma_i^i, \dot{\varepsilon}_0^p, \varepsilon_0^p$	Constants depending on microplastic parameters and relevant to internal stress
L_g	Grain size
τ_d	Characteristic time for dislocation motions
A_p, B_p, C_p, D_p	Constants relevant to microplastic flow
V, \dot{V}	Void volume and its rate of change
x^*, k, f^*	Reference values in the porous medium plasticity law
L	Pile-up length
τ^*, τ_a, τ_f	Dislocation driving shear stress, resolved shear stress, and lattice friction stress
N_{di}, N_{di}^{pu}	Number of dislocations in a pile-up, and its average value
N_{di}^{cri}	Critical number of dislocations in a pile-up for new crack nucleation
Λ_{pu}	Number of pile-ups intersecting a reference surface
L_{pu}, ϱ_{pu}	Average spacing between pile-ups, and pile-up density
θ, ξ	Angle between wedge crack and pile-up plane, and angle between σ_1 and the pile-up plane
l_w	Wedge crack length
σ_w, τ_w	Normal and shear stresses acting on the wedge crack
γ_s	Surface energy of the material

constant strain rate loading. All the parameters used thereafter can be found in Table 1.

In this paper, compressive stresses and compactive strains are counted positive. The principal stresses will be denoted σ_1 and σ_3 , σ_1 being the highest principal stress. The mean stress σ_m and the von-Mises effective stress σ_e are $\sigma_m = \sigma_{kk}/3$ and $\sigma_e = \sqrt{(3/2)S_{ij}S_{ij}}$, respectively, S_{ij} being the deviatoric stress defined as $S_{ij} = \sigma_{ij} - \delta_{ij}\sigma_m$, where δ_{ij} is the Kronecker delta. Stress triaxiality x is defined as $x = \sigma_m/\sigma_e$ and differential stress ($\sigma_1 - \sigma_3$) is denoted Q .

2.1 Elastic moduli of the cracked and deformed solid

Cracks and porosity have an impact on elastic moduli of porous materials (Mackenzie 1950; Walsh 1965a,b). Elastic moduli increase when porosity is closed and decrease with crack density increase (Bristow 1960; Budiansky & O'Connell 1976). Indeed, although open microcracks represent an extremely small amount of

porosity, they are very compliant (Guéguen *et al.* 2009). In this model, voids are made-up of spheroidal pores and penny-shaped cracks. Effective elastic moduli are expressed as a function of the overall porosity and the open crack density ρ (e.g. Kachanov 1993; Shafiro & Kachanov 1997; Fortin *et al.* 2007). We use Budiansky & O'Connell's 1976 definition of crack density ρ_c :

$$\rho_c = \frac{1}{V} \sum_{i=1}^N c_i^3, \quad (1)$$

where c_i is the radius of the i th crack and N is the total number of cracks embedded in the representative elementary volume (REV) V . In the dry case, for an isotropic distribution of crack orientations, the shear modulus G and bulk modulus K of a medium containing spheroidal pores and cracks can be expressed as a function of the shear and bulk moduli of the crack- and porosity-free matrix, and its Poisson's coefficient (e.g. Kachanov 1993; Shafiro & Kachanov 1997). As open crack density increases by $\Delta\rho_c$ with respect to its initial value, elastic moduli (K, G) decrease with respect

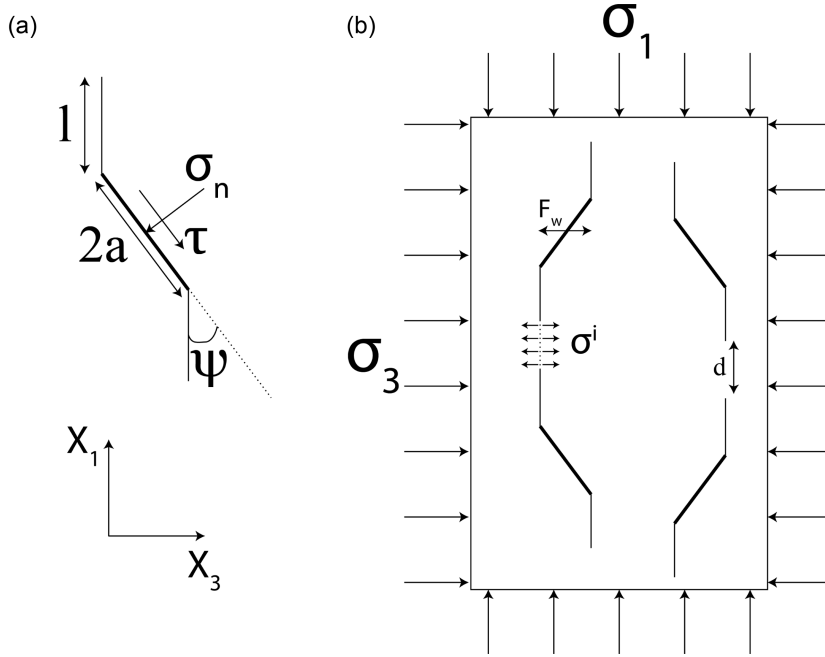


Figure 2. (a) An isolated wing-crack is subjected to remote stress. Wings develop from an initial flaw of radius a , parallel to σ_1 (direction X_1). (b) Geometry of the crack network used for the stress-intensity factor, K_I , calculated at a crack tip.

to their initial values (K_i , G_i). Note that here we neglect porosity variation, which is a fair approximation (e.g. Fortin *et al.* 2007). In the non-interaction approximation, evolution of K and G is given by (Appendix A):

$$\begin{aligned} \frac{G_i}{G} &\approx 1 + \Delta\rho_c \frac{h}{1 + \nu_i} \left(1 - \frac{\nu_i}{5}\right), \\ \frac{K_i}{K} &\approx 1 + \Delta\rho_c \frac{h}{1 - 2\nu_i} \left(1 - \frac{\nu_i}{2}\right), \end{aligned} \quad (2)$$

where G_i and K_i are the initial shear and bulk moduli, ν_i is the initial Poisson's coefficient and $\Delta\rho_c$ is the crack density variation during deformation. The factor h describes the penny-shaped geometry and is expressed as:

$$h = \frac{16(1 - \nu_i^2)}{9(1 - \nu_i/2)}. \quad (3)$$

When the model is used for rocks of known elastic moduli, experimental values can be used as initial values. When the model is used for rocks of unknown elastic moduli, their initial values can be computed with the rock initial crack density and porosity (Appendix A). Young modulus E and Poisson's ratio ν of the cracked porous medium are calculated from G and K .

Note that the overall crack orientations distribution may be anisotropic. In that case, the above calculations have to be extended to the anisotropic appropriate symmetry (Guéguen & Kachanov 2011). Moreover, in water-saturated cases, frequency dependence can be important and should be accounted for when determining elastic moduli from dynamic measurements (e.g. Adelinet *et al.* 2011; Fortin *et al.* 2014; Pimienta *et al.* 2015).

2.2 Macroscopic strains related to crack growth

Crack growth from a pre-existing isolated sharp inclined crack under compressive stresses can be described by wing crack models initially developed by Nemat-Nasser & Horii (1982), and later revisited by Ashby & Hallam (1986); Ashby & Sammis (1990);

Bhat *et al.* (2011, 2012); Mallet *et al.* (2015); Perol & Bhat (2016), among others. In their paper, Ashby & Sammis (1990) compared their theoretical predictions of failure envelopes to experimental data on granite, aplite, dunite, eclogite, gabbro, sandstone, limestone, marble and salt and showed that the agreement was excellent. Mallet *et al.* (2013) confirmed this good agreement using experiments performed on a cracked borosilicate glass.

We use Ashby & Sammis's approach to calculate the stress intensity factor K_I in a 3-D setting (Fig. 2). Isolated initial penny-shaped crack of radius a are inclined at an angle ψ with respect to the maximum principal stress (X_1 -axis; Fig. 2a). Wings of length denoted l can grow from each end of the pre-existing flaw, parallel to the X_1 -axis (Fig. 2a). Wing cracks form an array of interacting cracks in an isotropic linear elastic surrounding medium subjected to compressive stresses (Fig. 2b). The faces of the initial crack, in contact, can slide with some friction characterized by a Coulomb friction coefficient μ . The crack can also open, as discussed later. As wing cracks grow, the current damage increases. Current damage is defined as $D = (4/3)N_v\pi(l + a\cos\psi)^3$ (e.g. Ashby & Sammis 1990), where N_v is the number of cracks per unit volume. Initial damage is calculated with $l = 0$. The damage parameter D is not equivalent to the crack density as defined in eq. (1), because damage takes into account open and closed cracks whereas crack density only considers open cracks (e.g. Kachanov & Sevostianov 2012). If all cracks are open, damage and crack density become related and $D = (4/3)\pi\rho_c$. This current damage parameter does not take into account new cracks that are nucleated during the experiment. Damage due to new cracks is discussed in Section 2.4.

Subcritical crack growth is not considered here and cracks grow when the stress intensity at their tips K_I exceeds the fracture toughness K_{IC} of the solid. Thus, the condition for crack growth is:

$$K_I \geq K_{IC}. \quad (4)$$

Then, cracks propagate until K_I falls to K_{IC} . Under compressive stresses as considered in this study, K_I decreases as l increases until

the cracks start to interact strongly: each increment of crack advance requires an increment of load and growth is stable.

The previous condition for crack propagation is valid when (i) frictional sliding is enabled by the stress conditions, and (ii) the flanks of the initial crack remain in contact. Three regimes need to be considered (Deshpande & Evans 2008):

Regime I: Relative sliding on the flanks of the initial crack cannot take place because of friction, preventing cracks from growing. Damage remains at its initial value D_0 and open crack density is 0 because pre-existing cracks are closed.

Regime II: Relative sliding is possible and Ashby & Sammis's approach is used. Expression of the stress intensity K_I at the tip of interacting cracks forming an array is given by eq. (26) in Ashby & Sammis (1990). Damage increases as wing cracks propagate and $D = (4/3)N_v\pi(l + a \cos \psi)^3$. Crack density also increases and is equal to $\rho_c = 2N_v l^3$ because the wings are open but the flanks of the pre-existing flaws remain in contact.

Regime III: Contact between the flanks of the initial crack is lost and the current damage is directly linked to the open crack density: $D = (4/3)\pi \rho_c$. The situation reduces to the classical problem for a cracked elastic solid (Bristow 1960; Budiansky & O'Connell 1976; Tada *et al.* 2000). For an isotropic distribution of cracks, K_I^2 is a quadratic function of the stresses σ_m and σ_e :

$$K_I = [\pi a(C^2\sigma_m^2 + F^2\sigma_e^2)]^{1/2}, \quad (5)$$

where C and F are given in Deshpande & Evans (2008) and recalled in Appendix B, and depend on the initial damage D_0 and current damage D .

Based on elastic strain ε_{ij} continuities between regimes II and III, Deshpande & Evans (2008) found that the transition between regime II and regime III occurs at a stress triaxiality:

$$\varepsilon_{II \rightarrow III} = \frac{AB}{C^2 - A^2}, \quad (6)$$

where A and B depend on the initial and current damage and are given in Deshpande & Evans (2008) and recalled in Appendix B.

Strains at the macroscale ε_{ij} due to microcracks are calculated from the strain energy density W via the work conjugate relation (Deshpande & Evans 2008):

$$\varepsilon_{ij} = \frac{\partial W}{\partial \sigma_{ij}}. \quad (7)$$

Regime I: As cracks are closed and their flanks cannot slide, they have no influence on the elastic response of the solid.

Regime II: Noting ΔW the strain energy per crack, the strain energy density due to wing crack growth is $W = N_v \Delta W$. It is given by Deshpande & Evans (2008):

$$W = \frac{\pi D_0}{4\alpha^3 G_u (1 + \nu_u)} (A\sigma_m + B\sigma_e)^2, \quad (8)$$

where ν_u and G_u are the Poisson's ratio and the shear modulus of the uncracked porous medium (see Appendix A) and $\alpha = \cos \psi$.

Regime III: Contact is lost between the two sides of the pre-existing penny-shaped cracks and cracks open. Total strain energy density due to crack growth is (Deshpande & Evans 2008):

$$W = \frac{\pi D_0}{4\alpha^3 G_u (1 + \nu_u)} (C^2\sigma_m^2 + F^2\sigma_e^2). \quad (9)$$

To summarize, the parameters needed to describe the strain due to crack growth are the elastic constants of the matrix (G_0 and ν_0 or any equivalent doublet), porosity (needed to calculate the elastic moduli of the uncracked porous medium; G_u , $\nu_u = f(G_0, \nu_0, p)$;

see Appendix A), the initial damage D_0 , the size of pre-existing flaws a , the friction coefficient on these pre-existing cracks μ , and the fracture toughness of the solid K_{IC} . A discussion on the values taken by all these parameters is provided in Section 3.2.

2.3 Macroscopic strains related to intracrystalline plasticity

In low-porosity carbonate rocks deformed at low temperature, the microplasticity can account for the compactant ductile behaviour (e.g. Fredrich *et al.* 1989, 1990; Miguel *et al.* 2001). Mechanical twinning and r-, f-dislocation glide are accessible at low temperature and relatively low confining pressures in calcite (Turner *et al.* 1954; Griggs *et al.* 1960; De Bresser & Spiers 1997). Twinning and dislocation glide can be associated (e.g. Keith & Gilman 1960; Startsev *et al.* 1960; Braillon & Serughetti 1976) and occur simultaneously (e.g. Nicolas *et al.* 2017). Fig. 3 shows microstructural observations done on Tavel limestone deformed in the semi-brittle regime at $P_c = 70$ MPa (Nicolas *et al.* 2017). Dislocations and twins can be observed in deformed grains. Both mechanisms are microscopic plastic flow without volumetric change at the scale of the grains (Paterson 1978; Paterson & Wong 2005) that lead to a ductile behaviour at the macro-scale. However, for both mechanisms, plastic flows are imperfect in the sense that neither twins nor dislocations can be eliminated at low temperature. At low temperature, their density increases with the imposed deformation, leading to hardening. Thus, twinning and dislocation glide lead to similar macroscopic behaviours: ductile deformation with hardening. The aim of this section is to describe microplasticity with hardening. It would be possible to use a description based on twinning and/or dislocation glide. However, dislocation glide and twins may have different stress and strain sensitivity (e.g. Karato 2008). For simplicity we only consider dislocation glide here.

To describe the evolution of plastic strain rate $\dot{\varepsilon}^p$ as a function of the stress state, previous authors have used an empirical stress-dependent power law (e.g. Xiao & Evans 2003):

$$\dot{\varepsilon}^p = \dot{\varepsilon}_0 (\sigma / \sigma_p)^n, \quad (10)$$

where $\dot{\varepsilon}_0$ and σ_p are reference values, σ is the applied compression stress, and n is a material constant. A discussion of this macroscopic power-law description can be found in Renner & Evans (2002) and alternative constitutive relations can be found in Poirier (1985). In Appendix C, a micromodel accounting for dislocations-induced plastic flow and hardening is developed, leading to a physical description of eq. (10). Enhanced ductility in front of the crack tip due to stress concentrations and associated high dislocation density is not considered in this model. The reference stress σ_p is assumed to account for the material hardening and following Danas & Castañeda (2012), the matrix phase is assumed to exhibit an isotropic strain hardening law described as:

$$\sigma_p = \sigma_p^i \left[1 + \frac{\varepsilon^p}{\varepsilon_0} \right]^M, \quad (11)$$

where σ_p^i and ε_0 denote the initial yield stress and yield strain of the matrix material, respectively. The strain hardening exponent is taken as: $M \leq 1$. Using the micromodel accounting for dislocation-induced plastic flow and hardening, it is possible to justify that $M = 1/2$ and that $\varepsilon_0 = b L_g \rho_{id}^{\text{init}}$, where b is Burgers vector for calcite, L_g is the grain size, and ρ_{id}^{init} is the initial immobile dislocation density (see Appendix C). From the micromodel, the initial immobile dislocation density is directly linked to σ_p^i (see Appendix C).

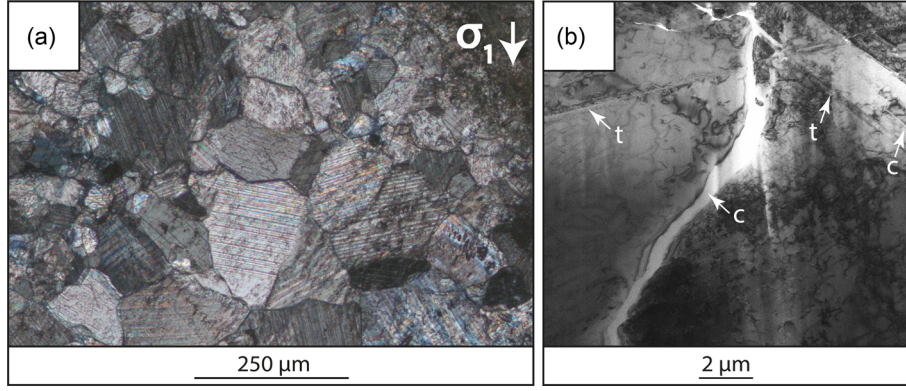


Figure 3. Micrographs of Tavel limestone samples deformed at 70 MPa and presented in Nicolas *et al.* (2017). (a) Micrograph of the sample under optical light. The twinning activity is very intense. (b) Observation of a foil milled in a highly twinned grain. At some point of inelastic compaction, crystals cannot undergo more plastic strain and develop intragranular cracks noted ‘c’. Dislocations and twins (noted ‘t’) are associated and occur simultaneously. Cracks are cross-cutting the twins.

Thus, at this stage, three parameters are needed to describe the evolution of plastic strain: $\dot{\epsilon}_0$, n , and σ_p^i . These three parameters will be discussed in Section 3.3.

The above plastic law is applicable to a non-porous medium. Dislocation glide does not lead to volumetric strain of the solid medium, but can induce porosity changes (and thus volumetric strain) of the porous material. Rice & Tracey (1969) first treated the ductile growth of voids as a problem of continuum plasticity by considering the asymmetric deformation of spherical voids embedded in an elastically rigid and incompressible plastic material. Budiansky *et al.* (1982) later accounted for nonlinear viscosity. Baud *et al.* (2000) modelled the inelastic compaction of a 3 per cent-porosity limestone at room temperature using a plastic pore collapse model (Curran & Carroll 1979). Xiao & Evans (2003) reproduced general trends of the deformation of a porous calcite-quartz aggregate at high temperature with a model of an isolated equivalent void in an incompressible nonlinear viscous matrix. Following these works, we use a creep model (Budiansky *et al.* 1982) to analyse the inelastic compaction at a macroscale. The porous rock is modelled as a medium containing isolated equivalent voids. Each void is assumed to be spherical and its surface to be traction-free.

As we focus on the mechanical behaviour of carbonate rocks under differential stress (i.e. shear-enhanced compaction), plasticity is set to 0 for high triaxiality ($|x| > 1$) when the stress state is close to hydrostatic, and thus inelastic compaction does not occur without shear stress. For low triaxiality ($|x| < 1$), plasticity develops (enabling shear-enhanced compaction). Based on the numerical results of Budiansky *et al.* (1982), Duva & Hutchinson (1984) derived an approximate normalised dilation rate:

$$\frac{\dot{V}}{\dot{\epsilon}V} = k(n)[x - x^*(n)], \quad (12)$$

where V is void volume, \dot{V} the rate of change of volume and $\dot{\epsilon}$ the remote volumetric strain rate. Values of k and x^* depend on n (defined through eq. 10) and are listed in Table 2. Duva & Hutchinson (1984) derived an approximate constitutive relation for the creep rate at low triaxiality:

$$\dot{\epsilon}_{ij}^{mp} = \frac{3}{2}\dot{\epsilon}_0 \left(\frac{\sigma_e}{\sigma_p}\right)^{n-1} \frac{S_{ij}}{\sigma_p} + p\dot{\epsilon}_0 \left(\frac{\sigma_e}{\sigma_p}\right)^n \times \left\{ \frac{3}{2} \left[(n+1)f^* + \frac{1}{2}k(n-1)x^2 \right] \frac{S_{ij}}{\sigma_e} + \frac{1}{3}kx\delta_{ij} \right\}, \quad (13)$$

Table 2. Values considered in the plasticity law for a porous medium that are taken from Duva & Hutchinson (1984).

n	f^*	x^*	k
1	0.833	0	2.25
1.5	0.965	−0.019	2.42
2	1.05	−0.031	2.55
3	1.16	−0.045	2.71
5	1.26	−0.058	2.88
10	1.35	−0.070	3.06
∞	1.46	−0.083	3.30

where p is the overall porosity. Values of f^* depend on the strain rate exponent n and are listed in Table 2. Note that eq. (13) is simply a new form of eq. (10) accounting for porosity p (second term in eq. 13). As the differential stress is increased, eq. (13) is resolved (allowing to calculate $\dot{\epsilon} = \dot{\epsilon}_{ii}^{mp}$) and then porosity is updated using the strain rate of the voids \dot{V} provided by eq. (12). The new plastic creep strain rate is then calculated with eq. (13). At this stage, porosity p is the only supplementary parameter appearing in eq. (13) needed additionally to the three parameters appearing in eq. (10).

In this study, pores are idealized as spheres. The initial shape and evolution of pores probably has a substantial effect upon the behaviour of the porous solid. However, a model accounting for other pore shapes is beyond this work.

The general formulation of eq. (13) is equivalent to considering the matrix material as an incompressible, nonlinearly viscous material (Renner & Evans 2002). When $n = 1$, the material is linearly viscous whereas when $n \rightarrow \infty$, it is rigid-perfectly plastic. The real situation is likely to be between these two end-members, which is discussed in Section 3.3.

2.4 Crack nucleation from pile-ups

At low temperature, in calcite, dislocation and twin slips are blocked at grain boundaries and defects, resulting in pile-ups (Fig. 3). These pile-ups create local stress concentrations that can be sufficient to nucleate new cracks (e.g. Stroth 1954, 1957; Smith & Barnby 1967; Olsson & Peng 1976; Wong 1990), as illustrated by Fig. 3(b). Thus, at low temperature, microplastic deformation can induce cracking and the two micromechanisms reported in Sections 2.2 and 2.3 are coupled. As for the intra-crystalline plasticity, only dislocations are considered here (see Section 2.3) but twins could also be considered

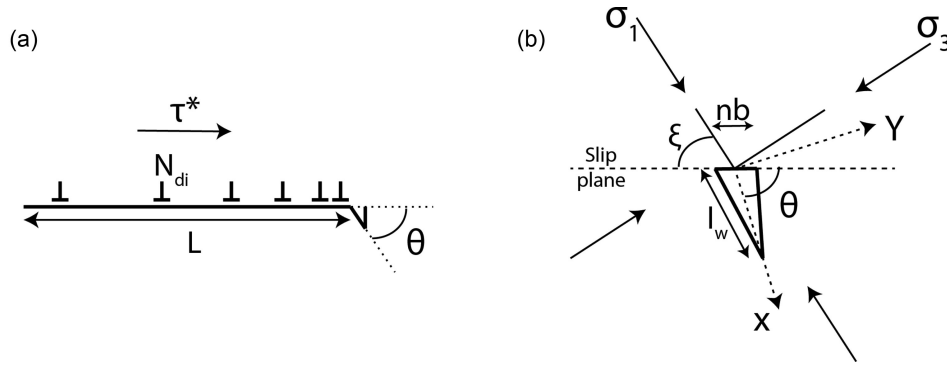


Figure 4. (a) A pile-up of N_{di} positive edge dislocations (Burger vector magnitude b) nucleating a tensile microcrack on a plane at an angle θ . The length of the pile-up is L . The driving shear stress is τ^* . (b) The wedge crack length is l_w , and the wedge opening at one end is nb due to the coalescence of n dislocations of Burger vector b . The remotely applied 2-D stress field has principal components σ_1 and σ_3 with the maximum principal compressive stress at an angle ξ to the dislocation pile-up.

because deformation due to twins is limited at low temperature, which creates local stresses sufficient to nucleate new cracks (e.g. Olsson & Peng 1976).

Considering a dislocation pile-up of length L (Fig. 4), Wong (1990) found the following condition for crack nucleation:

$$K_{IC} = \frac{4\sqrt{2}}{\sqrt{3\pi}} \tau^* \sqrt{L}, \quad (14)$$

where the driving shear stress is $\tau^* = \tau_a - \tau_f$, where τ_a and τ_f are the resolved shear stress and lattice friction stress, respectively. Following Eshelby *et al.* (1951), the number of dislocations N_{di} contained in a pile-up is:

$$N_{di} = \frac{\pi(1 - \nu_0)L\tau^*}{bG_0}, \quad (15)$$

where G_0 and ν_0 are the shear modulus and Poisson's ratio of the non-porous medium (calcite), respectively. Considering pile-ups of length $L = L_g/2$ and using eqs (14) and (15), the critical number of dislocations in the pile-up N_{di}^{crit} to nucleate a crack is:

$$N_{di}^{crit} = \frac{\pi\sqrt{3\pi}L_g}{8Gb_0}(1 - \nu_0)K_{IC}. \quad (16)$$

New crack nucleation will occur when the number of dislocations per pile-up N_{di}^{pu} reaches N_{di}^{crit} . Immobile dislocation (i.e. dislocations trapped in pile-ups) density is linked to the plastic strain undergone by the medium (eq. C8 in Appendix C). Dislocation densities represent average values whereas crack nucleation is controlled by high local concentration of dislocations in pile-ups (eq. 16). To deal with these complexities, let us separate dislocations into mobile and immobile ones: $\rho_d = \rho_{md} + \rho_{id}$, where ρ_{md} and ρ_{id} are mobile and immobile dislocation densities, respectively. Details are given in Appendix C. It is possible to find relations between immobile dislocation density and high local concentration of dislocations in pile-ups. A simplified model assumes that the overall immobile dislocation density is approximately given by the largest pile-ups. The number of immobile dislocations intersecting a surface S is:

$$N_{di} = \rho_{id}S. \quad (17)$$

If Λ_{pu} is the number of largest pile-ups over the area S , then the average number of dislocations per pile-up is:

$$N_{di}^{pu} = \frac{\rho_{id}S}{\Lambda_{pu}}. \quad (18)$$

Defining L_{pu} as the average spacing between pile-ups, the number of pile-ups intersecting the surface S is:

$$\Lambda_{pu} = \frac{S}{L_{pu}^2}. \quad (19)$$

The density of pile-ups is then defined as $\varrho_{pu} = 1/(L_{pu})^2$. This pile-up density is likely to be linked to the crystalline network of calcite, as discussed later. Combining eqs (18) and (19), the number of dislocations per pile-up is:

$$N_{di}^{pu} = \frac{\rho_{id}}{\varrho_{pu}}. \quad (20)$$

Using eq. (16), the condition for nucleating new cracks becomes:

$$\rho_{id} = \varrho_{pu} \frac{\pi\sqrt{3\pi}L_g}{8G_0b}(1 - \nu_0)K_{IC}. \quad (21)$$

Following Wong (1990), the mode I stress intensity factor of the wedge crack nucleated by a dislocation pile-up can be calculated as:

$$K_I = \frac{G_0N_{di}^{pu}b}{(1 - \nu_0)} \frac{\sin\theta}{\sqrt{2\pi l_w}} - \sigma_w \sqrt{\pi l_w/2}, \quad (22)$$

where θ is the angle between the wedge crack and the pile-up plane (Fig. 4b), l_w is the length of the wedge crack and $\sigma_w = (\sigma_1 + \sigma_3)/2 - (1/2)(\sigma_1 - \sigma_3)\cos(2[\theta - \xi])$ is the resolved normal stress acting on the wedge crack. In this last expression, ξ is the angle between the maximum principal stress and the pile-up plane (Fig. 4b). Following Wong (1990), the angle θ is taken equal to 70.5° (maximum hoop stress) and ξ to 45° (maximum resolved shear stress). Then, the condition for wedge crack propagation is described by eq. (4): cracks propagate until K_I (calculated with eq. (22)) falls to K_{IC} . Once nucleated, cracks can propagate across crack boundaries and become larger than the grain size.

The volumetric strain induced by wedge cracks is calculated with eq. (7). The free energy change ΔW due to the wedge crack is (Wong 1990):

$$\Delta W = \frac{\pi(1 - \nu_0^2)}{4G_0}(\sigma_w^2 + \tau_w^2)l_w - 2\gamma_s, \quad (23)$$

where τ_w is the shear stresses acting on the wedge crack, and γ_s is the surface energy. Deriving this expression with respect to σ_{ij} , the volumetric strain due to wedge cracks is:

$$\varepsilon_{vol}^{wc} = (1 - \nu_0) \frac{\pi(1 - \nu_0^2)l_w}{2G_0} [\sigma_1 \cos^2(\theta - \xi) + 2\sigma_3 \sin^2(\theta - \xi)]. \quad (24)$$

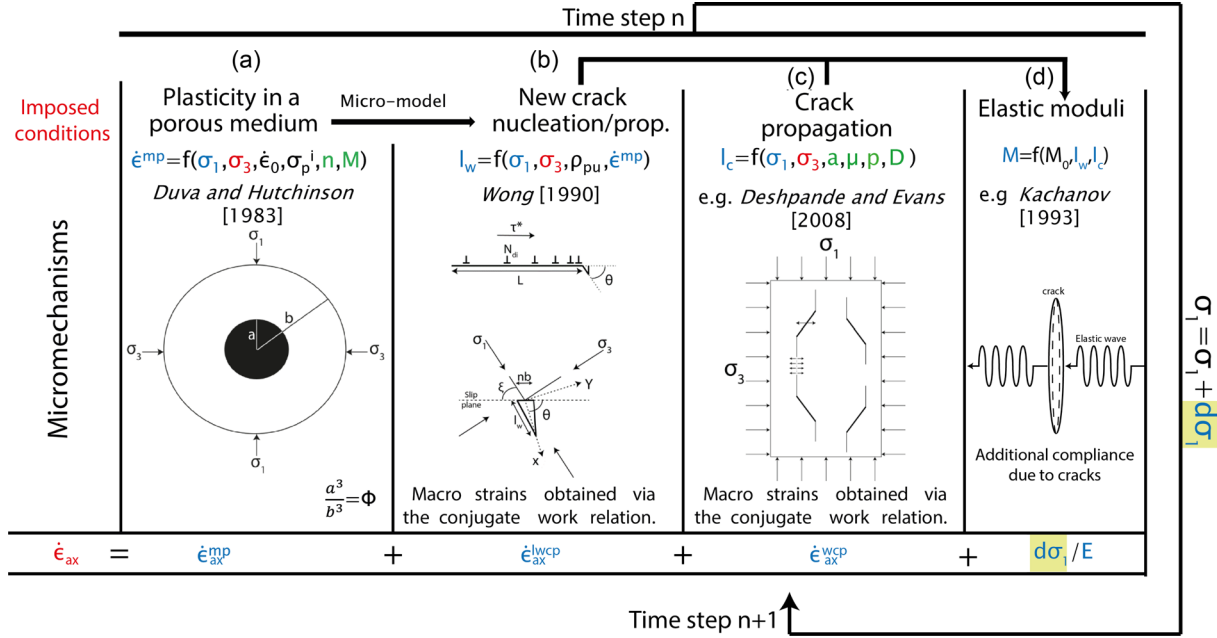


Figure 5. Illustration of the phenomena taken into account in the model. Parameters in red are those imposed, parameters in green are taken from the literature, parameters in black are inverted and parameters in blue are calculated and vary throughout the calculations. (a) Intracrystalline plasticity leads to plastic pore collapse. (b) The intracrystalline plasticity can be calculated in terms of dislocation glide. Dislocation pile-ups can induce new crack nucleations. (c) Wing cracks develop from an initial flaw parallel to σ_1 and interact. (d) Crack nucleation and propagation induce a decrease of elastic moduli. The imposed axial strain rate is accommodated by plastic pore collapse (a), new crack nucleation due to pile-ups (b), crack propagation from pre-existing flaws (c), and elastic deformation calculated with varying moduli and increasing differential stress (d).

The current damage due to new cracks is:

$$D_w = \varrho_{pu}^{3/2} l_w^3. \quad (25)$$

Thus, at this stage, one parameter is needed to describe the propagation of wedge cracks: ϱ_{pu} . This parameter will be fitted to experimental data, which is discussed in Section 4.2.1.

2.5 Stress–strain relation during constant strain rate deformation

The overall stress–strain curve of the porous material submitted to a constant strain rate can finally be derived from the previous steps. Total strain is the sum of (i) the elastic strain, (ii) the strain induced by cracks propagating from pre-existing flaws (Section 2.2) and induced by plasticity (Section 2.4) and (iii) the microplasticity-induced (Section 2.3) strains. During a short time dt , total strain $d\epsilon$ is:

$$d\epsilon = d\epsilon^e + d\epsilon^{\text{cracks}} + d\epsilon^{mp}, \quad (26)$$

where $d\epsilon^e$, $d\epsilon^{\text{cracks}}$ and $d\epsilon^{mp}$ are the elastic, crack propagation and porous material microplastic strain increments, respectively. Total axial strain is $d\epsilon_1 = \dot{\epsilon}_1 dt$, where $\dot{\epsilon}_1$ is the imposed constant axial strain rate. The crack and microplastic axial strains are calculated with the work conjugate relation and eq. (13), respectively. Then, the macroscopic axial stress increment $d\sigma_1$ is:

$$d\sigma_1 = E d\epsilon_1^e, \quad (27)$$

where E is the evolving Young modulus of the cracked porous medium (Section 2.1) and $d\epsilon_1^e$ the elastic axial strain increment. This incremental procedure is repeated to obtain the entire constitutive stress–strain relation.

3 SUMMARY OF THE MODEL, CHOICE OF MATERIAL PROPERTIES AND SENSITIVITY TO THESE PARAMETERS

3.1 Summary of the equations used in computation of the model

In this section, we detail the equations used when computing the model. The overall procedure is shown in Fig. 5. At each given time step, we proceed in the following way:

(1) *Kinetic of wing crack propagation:* Based on the stress state, we examine if sliding on pre-existing flaws is possible. If no, crack is not propagated. If yes, stress triaxiality is calculated and compared to that of the transition between regime II and III (eq. 6). Depending on the regime, K_I is calculated with eq. (26) from Ashby & Sammis (1990) or with eq. (5). If K_I is lower than K_{IC} , wing cracks do not propagate. Otherwise, wing crack length is increased until K_I becomes lower than K_{IC} . Strains related to crack growth are calculated with eq. (7).

(2) *Kinetic of intracrystalline plasticity and plastic pore collapse:* Then, plastic pore collapse is calculated. eq. (13) is resolved (allowing to calculate $\dot{\epsilon} = \dot{\epsilon}_{ii}^{mp}$) and then porosity is updated using the strain rate of the voids \dot{V} provided by eq. (12). The yield stress of the plasticity law is finally updated following eq. (11). The number of immobile dislocations is calculated with eq. (C8) provided in Appendix C.

(3) *Kinetic of cracks induced by pile-ups:* Under the assumptions discussed in Section 2.4, the density of immobile dislocations is compared to the condition for new crack nucleation expressed by eq. (21). If the density of immobile dislocations is higher than the threshold expressed by eq. (21), the length of nucleated cracks l_w is increased until K_I expressed by eq. (22) falls below K_{IC} . Finally, the volumetric strain due to nucleated cracks is calculated with

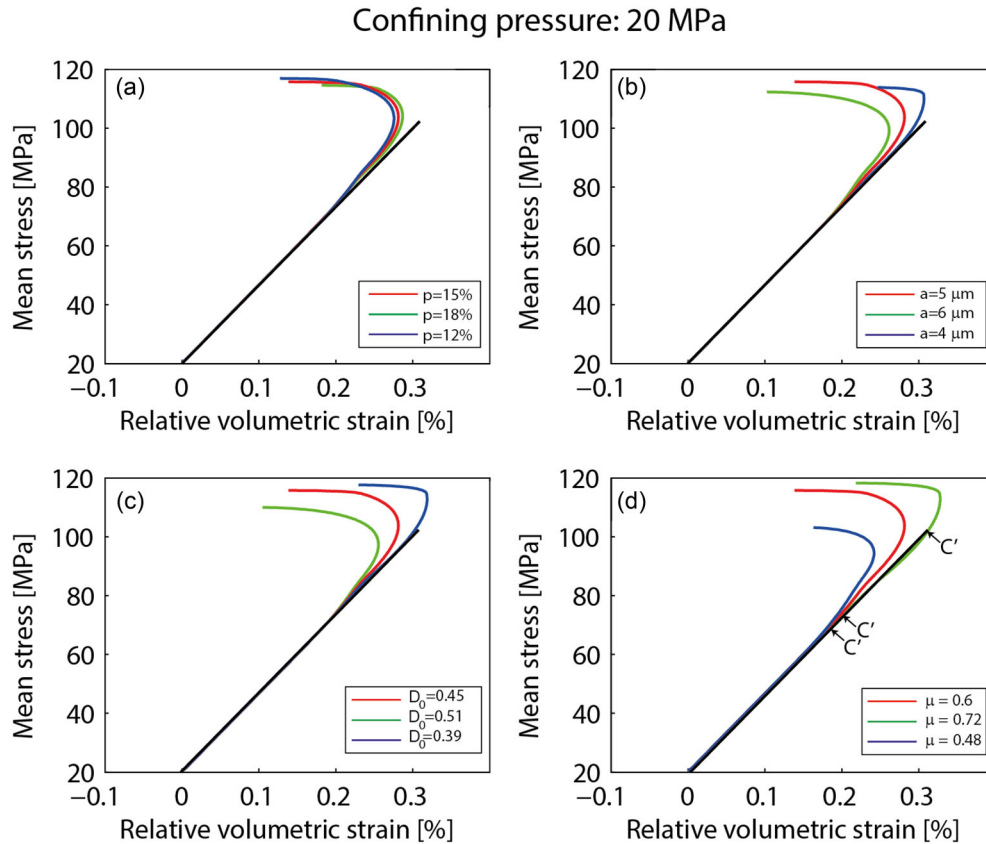


Figure 6. Influence of the input parameters characterizing the brittle behaviour. The model is run for a confining pressure of 20 MPa. Each parameter is changed by 20 per cent around an average value. (a) Influence of a 20 per cent variation of porosity around the average value $p = 15$ per cent. (b) Influence of a 20 per cent variation of initial penny-shaped crack radii around the average value $a = 5 \mu\text{m}$. (c) Influence of a 20 per cent variation of the initial damage around the average value $D_0 = 0.45$. (d) Influence of a 20 per cent variation of the friction coefficient on the initial penny-shaped cracks around the average value $\mu = 0.6$. Arrows represent the onset of dilatancy C' for each value of friction coefficient.

eq. (24) and the damage due to new cracks is calculated with eq. (25) and converted into crack density (cracks are open).

(4) The next step is to update the elastic moduli, simply with eq. (2) and taking into account crack density due to new cracks and open wing cracks. Concerning the wing cracks, depending on the regime, the open crack density is related to the damage as discussed in Section 2.2.

(5) Once everything is calculated for the given time step, the change of axial stress is calculated with eq. (27) and the same procedure is applied for the next time step.

3.2 Parameters relevant to elastic properties and crack propagation

In this section, we detail the parameters relevant to describe a brittle behaviour. Calcite Young's modulus $E_0 = 84 \text{ GPa}$ and Poisson's ratio $\nu_0 = 0.28$ are taken from Homand *et al.* (2000). Any other set of independent elastic constants of calcite are calculated from these values. If elastic moduli of the initial cracked porous medium (G_i , K_i or any other set of independent elastic constants) are known, eq. (2) is used to compute the evolution of the elastic constants as a function of the evolution of damage (crack density). If the initial elastic moduli of the medium are unknown, they can be computed using the initial porosity and crack density of the material (e.g. Fortin *et al.* 2007). Elastic moduli of the uncracked porous medium are calculated using calcite moduli and porosity (e.g. Fortin *et al.* 2007).

Critical stress intensity factor is taken equal to $K_{IC} = 0.14 \text{ MPam}^{1/2}$, corresponding to a surface energy for dry calcite equal to $\gamma_s = 0.23 \text{ J m}^{-2}$ as measured by Gilman (1960). This is in good agreement with the value of $\gamma_s = 0.32 \text{ J m}^{-2}$ found by Røyne *et al.* (2011) for dry calcite and with values of K_{IC} around $0.2 \text{ MPam}^{1/2}$ reported by Atkinson (1984).

Crack density can be inferred from elastic wave velocity measurements (e.g. Sayers & Kachanov 1995; Fortin *et al.* 2005) or SEM images (e.g. Fredrich *et al.* 1989; Mallet *et al.* 2013). Typical values for intact carbonate rocks are in the range $[0-0.05]$. Crack mean size can be inferred from SEM images (e.g. Mallet *et al.* 2013) or taken as equal to the grain size. The friction coefficient on pre-existent penny-shaped cracks can be inferred from a linear failure envelope, assuming that friction is equal on a macroscopic fault and microcracks. Typical values for intact rocks are in the range $[0.4-0.8]$. Porosity can be measured using a triple weighting procedure or weighting the sample and assuming a 100 per cent calcite matrix. Typical values of porosity that the model is able to tackle are discussed in Section 4.3.

The influence of porosity, initial crack length, initial crack density and friction coefficient is explored hereafter (Fig. 6). The value of each parameter is varied by 20 per cent around an average value. Average values are taken equal to the set of parameters used in the comparison to white Tavel limestone and are given in Table 3. Porosity has a small influence on the model prediction (Fig. 6a). Initial penny-shaped crack radii and crack density have a strong influence

Table 3. Microstructural parameters used to predict the macroscopic mechanical behaviour of Solnhofen limestone at a confining pressure of 200 MPa and macroscopic mechanical behaviour of white Tavel limestone.

	Porosity per cent	D_0	a (μm)	μ	n	$\dot{\epsilon}_0$ s^{-1}	σ_p^i (MPa)	ϱ_{pu} (m^{-2})	K_i (GPa)	G_i (GPa)
Solnhofen limestone	3 ^a	0.25 ^a	5 ^a	0.53 ^a	10	2.5e-19 ^b	18 ^b	1e8 ^b	53 ^a	22.4 ^a
White Tavel limestone	15 ^c	0.45 ^c	5 ^c	0.6 ^c	10	2e-21 ^b	5 ^b	1.8e8 ^b	26.7 ^c	13 ^c

^aAfter Baud *et al.* (2000).

^bFitting data.

^cAfter Nicolas *et al.* (2016).

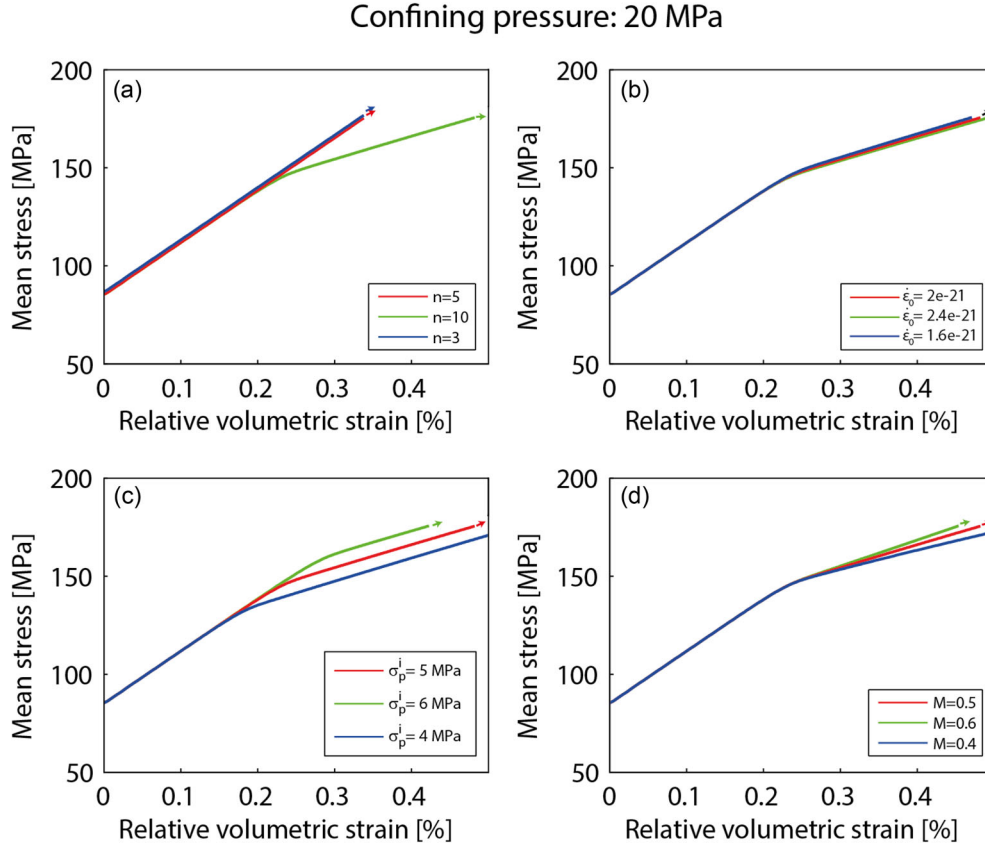


Figure 7. Influence of the input parameters characterizing the ductile behaviour. The model is run for a confining pressure of 85 MPa. (a) Influence of a variation of the stress sensitivity n . (b) Influence of a 20 per cent variation of the reference strain rate around the average value. (c) Influence of a 20 per cent variation of the initial yield stress σ_p^i around the average value. (d) Influence of a 20 per cent variation of the strain hardening exponent around the average value.

on the peak stress (Figs 6b and c). A variation of 20 per cent around the average value induces variations of 15 per cent in the predicted peak stress. Finally, the friction coefficient has the strongest influence (Fig. 6d). Its variation has a strong influence on the onset of dilatancy C' (represented by arrows), on the peak stress and on the volumetric strain at the peak stress. As the friction coefficient increases, the onset of dilatancy C' , the peak stress and the volumetric strain at peak stress increase.

3.3 Parameters relevant to plasticity and dislocations

The ductile behaviour of the matrix material is described by eqs (10) and (11) (with $M = 1/2$) and the ductile behaviour of the porous material is described by eq. (13). All parameters of the plasticity and hardening laws are microstructure-dependent. Grain size can be obtained from SEM images, shear-modulus is an elastic constant

provided by eq. (2). Burgers vector in calcite is $a_0 = 6.4 \times 10^{-10}$ m (De Bresser 1996).

For the non-porous matrix, the microparameters that need to be fixed *a priori* are the mobile and immobile dislocation densities (or equivalently $\dot{\epsilon}_0$ and σ_p^i) and the stress sensitivity n . In addition, for porous materials, porosity has to be known (eq. 13). The sensitivity of the model to each parameter is examined thereafter. The value of each parameter is varied independently. Stress sensitivity n has a strong influence on the inelastic compaction (Fig. 7a). When n is increased, inelastic compaction for a given stress level is enhanced. Models based on the motion of dislocations predict value in the region of 3 to 5 for n (e.g. Kirby & Raleigh 1973; Stocker & Ashby 1973; Weertman 1975). Schmid *et al.* (1977) measured values in the range 1.7–4.7 on Solnhofen limestone deformed at high temperature, Wang *et al.* (1996) measured values around 5 in calcite single crystals deformed at temperatures around 800 °C but higher values (4.2–10) were found on marbles (Heard & Raleigh 1972;

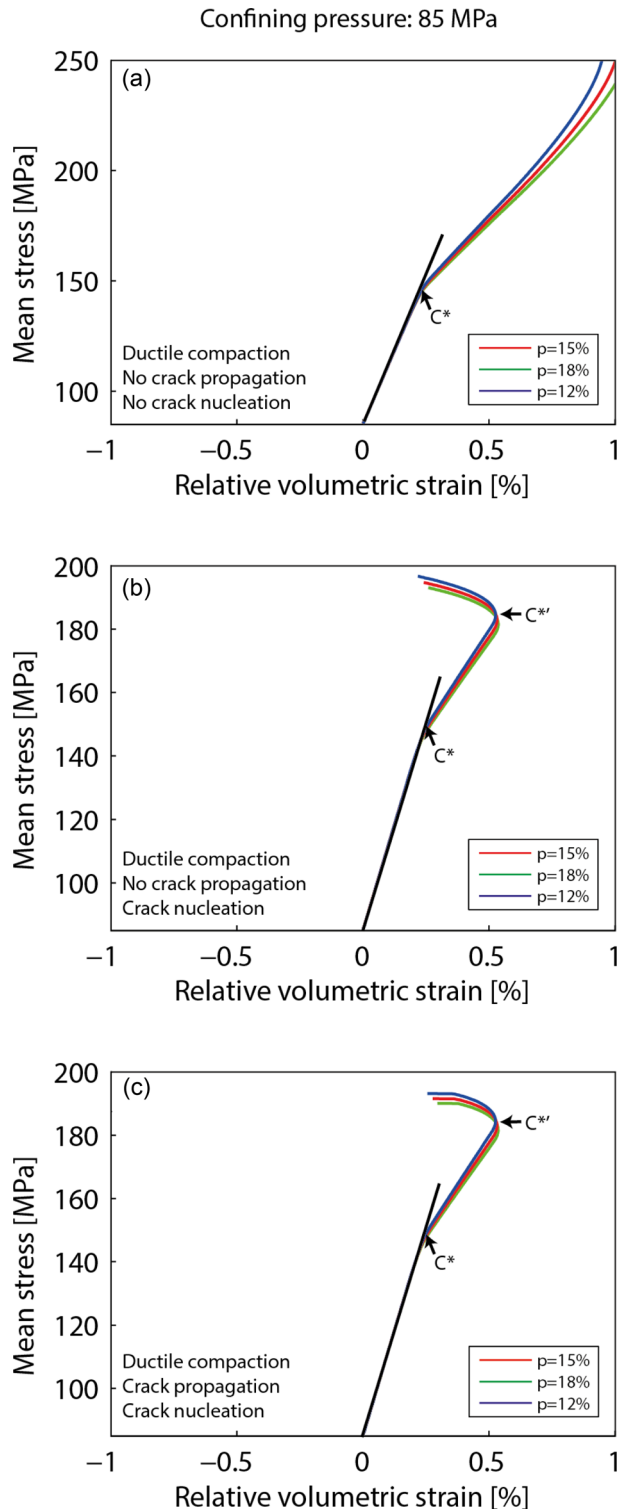


Figure 8. Influence of the porosity on the ductile behaviour. The model is run for a confining pressure of 85 MPa. The predicted onset on inelastic compaction (C^*) and post-yield onset of dilatancy ($C^{*'}$) are shown by arrows. (a) Influence of a 20 per cent variation of the porosity on the inelastic compaction. Pre-existing cracks cannot propagate. No crack nucleation is possible. (b) Influence of a 20 per cent variation of the porosity on the inelastic compaction and nucleation of new cracks. Pre-existing cracks propagate but their volumetric strain is not taken into account. Crack nucleation is possible. (c) Influence of a 20 per cent variation of the porosity on the inelastic compaction. Pre-existing cracks can grow and new cracks can nucleate.

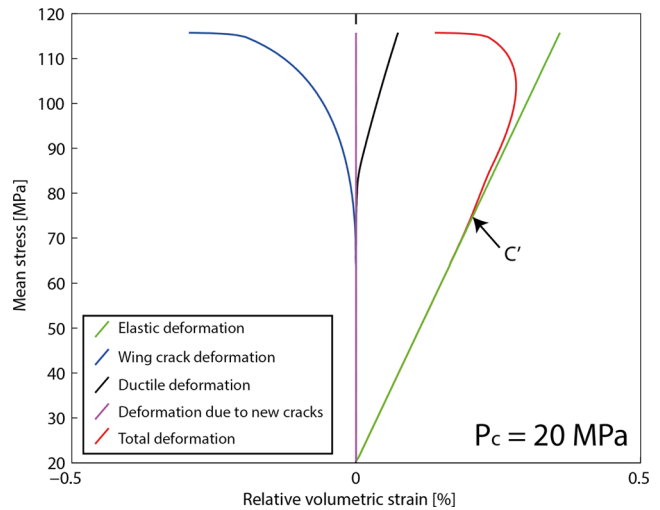


Figure 9. Model predictions for volumetric strain due to all the physical phenomena taken into account for a confining pressure of 20 MPa.

Rybacki *et al.* 2013). This difference could be due to some grain size effect (Schmid *et al.* 1977). The data from Renner *et al.* (2002) agree with a power law relation with a stress sensitivity $n = 4.5$ even though creep tests indicate that the stress exponent is actually not constant (Renner *et al.* 2002). However, their study focuses on high temperature deformation. At low temperature, n is likely to be higher (e.g. Rybacki *et al.* 2013) because the deformation regime is different from that at high temperature. Rybacki *et al.* (2013) found higher values for n in marble deformed at temperatures lower than 300 °C, in agreement with Rutter (1974) who found values around 15 for n for Solnhofen limestone, Carrara and Yule marbles deformed at low temperature. Thus, a standard constant value of $n = 10$ is used in this study.

When the reference strain rate $\dot{\epsilon}_0$ is increased by 20 per cent, volumetric strain rate increases but the effect remains very small (Fig. 7b). The initial yield stress σ_p^i has the exact opposite influence: when it is increased, volumetric strain tends to decrease and the onset of inelastic compaction to increase, but the effect is small (Fig. 7c). The strain hardening exponent M has been fixed at $M = 0.5$, which is physically justified in Appendix C. However, given its importance, the sensitivity to this parameter is also examined (Fig. 7d). When M is increased, volumetric strain tends to decrease (Fig. 7d). Finally, the influence of porosity on inelastic compaction, new crack nucleation and overall semi-brittle behaviour is examined hereafter (Fig. 8). Inelastic compaction rate increases with initial porosity (Fig. 8a). Porosity also has a small influence on the post-yield onset of dilatancy ($C^{*'}$), due to new crack nucleation (Fig. 8b). When porosity is increased, the onset of dilatancy takes place at a slightly higher volumetric strain and a slightly lower differential stress. Taking into account pre-existent crack propagation does not change these conclusions (Fig. 8c), but increases the dilatancy attained at rupture and decreases the peak stress (Figs 8b and c).

4 RESULTS AND DISCUSSION

4.1 Prediction of the stress/strain response

We investigate the model predictions for $\dot{\epsilon}_{ax} = 10^{-5} \text{ s}^{-1}$ and for the parameters of Tavel limestone given in Table 3. At a confining pressure of 20 MPa, no significant plastic flow and no crack nucleation take place (Fig. 9). The volumetric strain versus mean stress curves

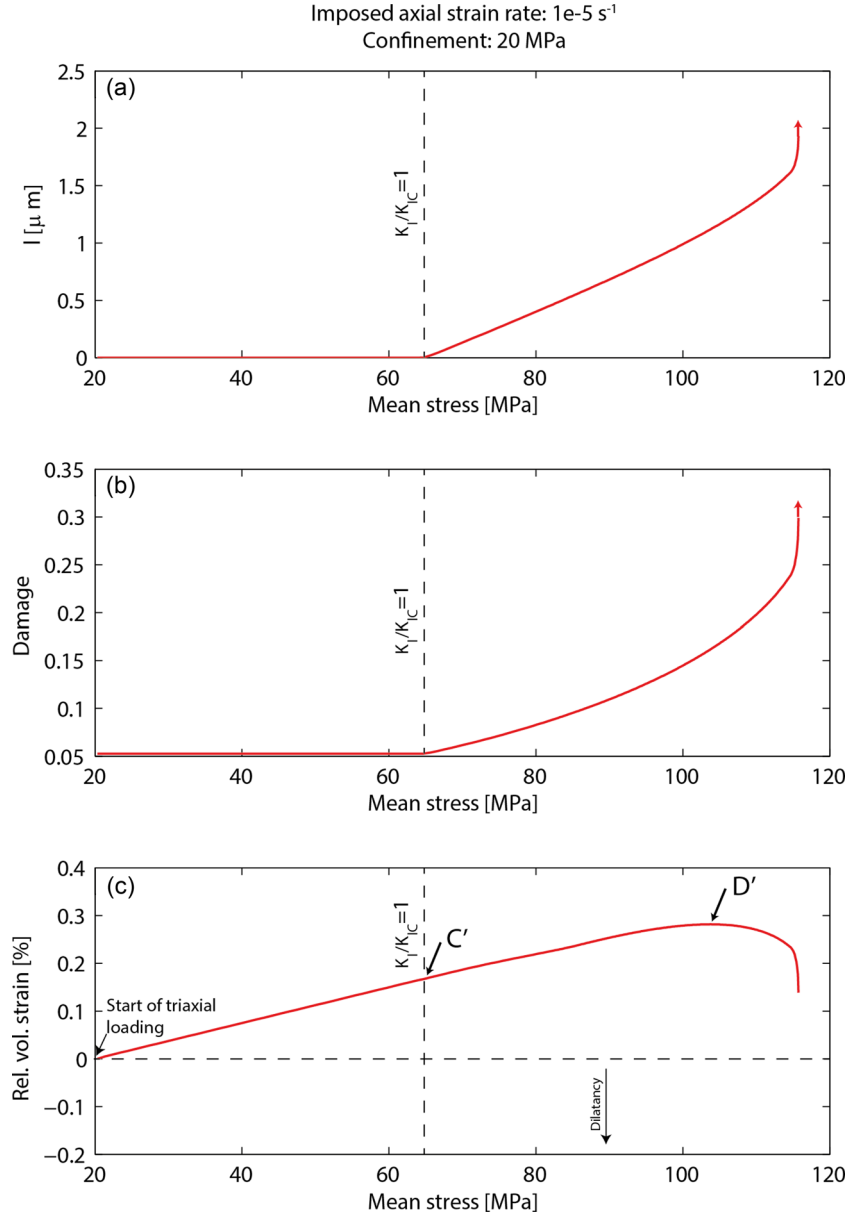


Figure 10. Mechanical parameters evolution during deformation at a confining pressure of 20 MPa. (a) Wing crack length l as a function of the mean stress P . The red arrow indicates the divergence of l that occurs at failure. (b) Damage evolution as a function of P . (c) Relative volumetric strain (i.e. volumetric strain is set to zero before the beginning of differential stress loading) as a function of P . The onset of dilatancy C' and predominance of dilatancy D' are shown for reference.

first show an elastic compactant behaviour until a critical stress state denoted C' (Wong *et al.* 1997) beyond which the volumetric strain deviates from elasticity because of the onset of dilatancy (Fig. 9). Elastic deformation and wing crack propagation are responsible for the major part of the total deformation. Details on the brittle behaviours are given in Fig. 10. At low mean stress, wing lengths remain at 0 (regime 1, friction prevents cracks from growing). At a given threshold, for a mean stress around 65 MPa, K_I/K_{IC} increases. When $K_I/K_{IC} = 1$, wing cracks start to grow, which leads to a dilatant component of the volumetric strain. The onset of dilatancy is marked by the stress state C' . At this point elastic compaction and crack propagation inducing dilatancy are taking place simultaneously but compaction is dominant. Dilation becomes dominant at a mean stress of about 100 MPa, marked D' . When cracks start to interact, dilatancy increases faster with the differential stress. At

macroscopic failure, K_I and wing crack lengths diverge, as marked by the red arrows. Macroscopic rupture is reached at a mean stress of approximately 115 MPa.

At a confining pressure of 85 MPa (Fig. 11), inelastic compaction takes place. At low differential stress, elastic deformation is responsible for the overall deformation (Fig. 11). At higher differential stress values, overall deformation undergoes shear-enhanced compaction (Baud *et al.* 2000) due to the onset of plasticity before it becomes dilatant because new cracks nucleate. Let us first examine porosity collapse assuming that neither crack nucleation nor crack propagation is possible (Fig. 12). At a given differential stress threshold, plastic strain rate increases sharply. This stress state denotes the onset of inelastic compaction C^* in the macroscopic behaviour. At this point, the normalised dilation rate (eq. 12) increases sharply, σ_p/σ_p^i start to increase because hardening is taking place

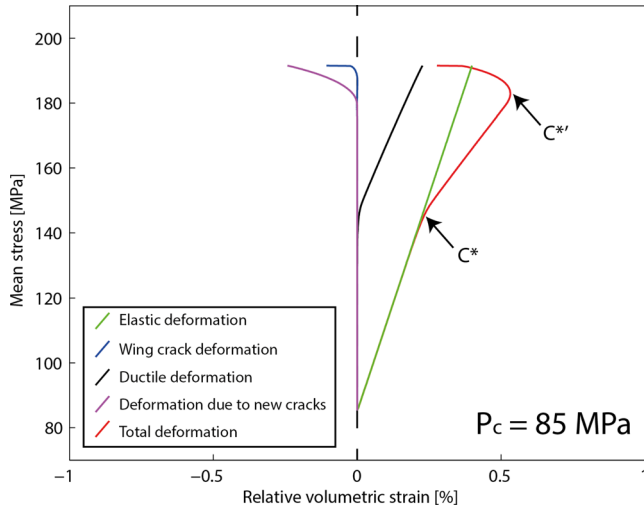


Figure 11. Model predictions for volumetric strain due to all the physical phenomena taken into account for a confining pressure of 85 MPa.

and porosity starts to decrease because of pore collapse. Beyond C^* , volumetric ductile strain rate decreases as σ_p/σ_p^i increases, because of hardening. Porosity decreases as a result of plastic pore collapse.

Let us now assume that new crack nucleation is possible due to dislocation pile-ups (Fig. 13). The dislocation density increase accelerates with σ_p/σ_p^i (Fig. 13a). At low σ_p/σ_p^i values, cracks cannot nucleate because the internal stress is not high enough. When dislocation pile-ups induce an internal stress high enough, new cracks nucleate, grow and reach a length of over five microns. Induced crack density and volumetric strain increase (Figs 13c and d). At rupture, nucleated dislocation density ρ_{id}^{new} is around $\rho_{id}^{new} = 4.5 \times 10^{12} \text{ m}^{-2}$, nucleated crack length is around 5 μm , crack density is almost 0.2 and dilatancy due to new cracks is almost 0.3 per cent. Note that these values are consistent: the nucleated dislocation density is comparable to observations on significantly deformed materials (e.g. Fredrich *et al.* 1989; Dimanov *et al.* 2007), crack length is of the order of the grain size and crack density is comparable to experimental results.

4.2 Comparison with available data

4.2.1 Mechanical data

Baud *et al.* (2000) performed constant strain rate deformation experiments on Solnhofen limestone. A detailed curve of the mechanical behaviour of Solnhofen limestone under differential stress is given in (Baud *et al.* 2000) for a confining pressure of 200 MPa. Porosity is composed of pre-existing microcracks (crack porosity 0.2 per cent) and equant pores (porosity 2.8 per cent). At this confining pressure, pre-existing microcracks are closed (Baud *et al.* 2000) but wing cracks can grow from pre-existing closed flaws. In the model, initial damage is described by a crack density and a crack initial length. Microstructural parameters ($\mu = 0.53$, $D_0 = 0.25$ among others) are given in Baud *et al.* (2000). Initial damage $D_0 = 0.25$ corresponds to an open crack density $\rho_c = 0.047$ (see the relation between D_0 and ρ_c in Section 2.2). Initial crack length is $l_c = 5 \mu\text{m}$ (grain size). The model is run with a porosity of equant pores of 3 per cent. Stress sensitivity n , and strain hardening exponent M are taken equal to 10 and 0.5, respectively. A discussion on the values of these parameters was provided in Section 3.3. Elastic constants are those experimen-

tally measured. The reference strain rate $\dot{\epsilon}_0$, the initial yield stress σ_p^i , and the pile-up density ρ_{pu} are fitted to retrieve the macroscopic behaviour measured experimentally. Their values can be found in Table 3. The onset of dilatancy is controlled by the pile-up density ρ_{pu} . To fit the data, it is found that $\rho_{pu} = 1 \times 10^8 \text{ m}^{-2}$. This value corresponds to about 1 pile-up over 23 grains of size 5 μm ; which is a realistic value. All parameters used can be found in Table 3.

The model closely reproduces the experimental stress–strain relation (Fig. 14). Predicted stress states C^* and $C^{*'}$ and corresponding volumetric strains are close to experimental ones, even if C^* is slightly overestimated. Once fitted on an experiment, the unknown parameters are determined and further model predictions can be compared to experimental results for other confining pressures.

Nicolas *et al.* (2016) performed constant strain rate deformation experiments on white Tavel limestone (porosity of 14.7 per cent). At $T = 70^\circ\text{C}$ and P_c lower than 55 MPa, the mechanical behaviour and failure mode are typical of the brittle faulting regime (Paterson & Wong 2005). At $T = 70^\circ\text{C}$ and P_c equal or higher than 55 MPa, the mechanical behaviour is semi-brittle and characterized by an elastic compaction beyond which an inelastic compactive regime takes place. At higher strain, dilatancy overcomes compaction. Mean stress versus volumetric strain is shown in Fig. 15(a) for various confining pressures.

Microstructural parameters ($\mu = 0.6$, $\rho_c = 3 \times 0.035 = 0.105$) are given in Nicolas *et al.* (2016). The friction coefficient was inferred from failure envelope (Nicolas *et al.* 2016) and initial crack length is set to $l_c = 5 \mu\text{m}$ (grain size, Nicolas *et al.* (2016)). Initial damage D_0 is set to 0.45, which corresponds to the initial crack density inverted from elastic wave velocities at low pressure (Nicolas *et al.* 2016) under the assumption that cracks were initially open. The model is run with a porosity of 15 per cent, very close to the experimentally measured value (14.7 per cent). Stress sensitivity n , and strain hardening exponent M are those used previously and are taken equal to 10 and 0.5, respectively (see Section 3.3 for discussion). Elastic constants are those experimentally measured. The reference strain rate $\dot{\epsilon}_0$, the initial yield stress σ_p^i , and the pile-up density ρ_{pu} are fitted to retrieve the macroscopic behaviour measured experimentally at the highest confining pressure (85 MPa). The reason is that they describe the semi-brittle behaviour observed at high confining pressure. Onset of dilatancy is controlled by the parameter ρ_{pu} , which represents the pile-up density. For these predictions, $\rho_{pu} = 1.8 \times 10^8 \text{ m}^{-2}$. This corresponds to about 1 pile-up over 15 grains of size 5 μm . All these parameters are obtained for one experiment (confining pressure of 85 MPa). Then, the same parameter values are used for modelling the behaviour at different confining pressures. All parameters used can be found in Table 3. To summarize, three parameters relevant to the semi-brittle behaviour (inelastic compaction and post-yield onset of dilatancy) are fitted to retrieve the behaviour of the sample deformed at the highest confining pressure. The same set of parameters is then used to predict the behaviour at all confining pressures.

Using parameter values reported in Table 3, predicted behaviour is reported in Fig. 15(b). Experimental and predicted stress–strain curves are very similar (Fig. 15). At confining pressures below or equal to 35 MPa, the predicted mechanical behaviour is brittle. Below the brittle-ductile transition, the model reproduces the general trend of the deformation. Stress states C' and peak stress are generally over estimated, which is probably due to a too small initial crack length. At confining pressures strictly above 35 MPa, the predicted mechanical behaviour is characterized by elastic compaction, transient inelastic compaction, ultimately leading to dilatancy. However, predicted stress states C^* and $C^{*'}$ (and related volumetric strains)

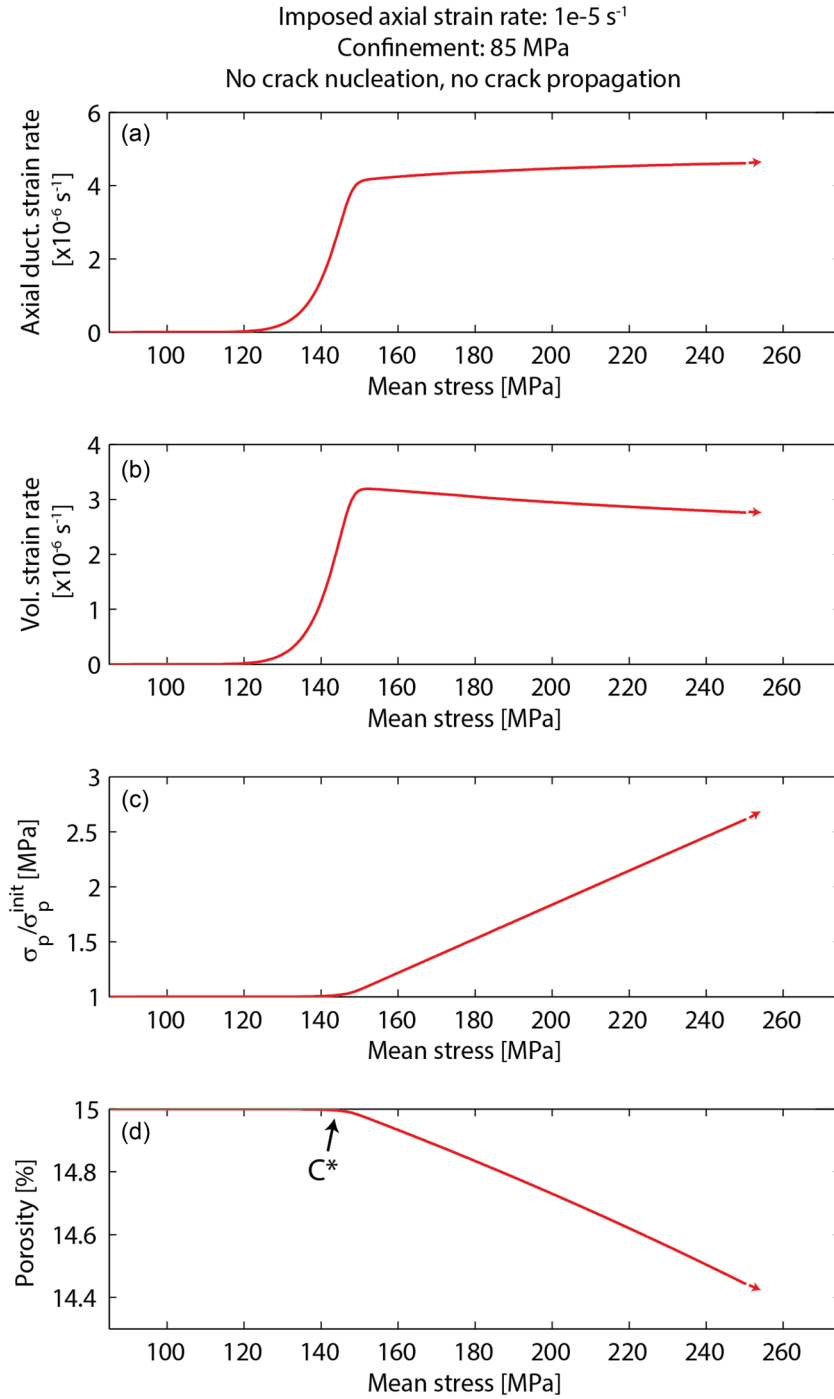


Figure 12. Compilation of mechanical parameters linked to the ductile behaviour. (a) Evolution of the axial ductile strain rate as a function of the mean stress P . (b) Evolution of the volumetric ductile strain rate as a function of P . (c) Reference stress in the plasticity law normalized by its initial value as a function of P . (d) Porosity evolution as a function of P .

are very close to experimental ones (less than 20 percent difference). The inferred brittle-ductile transition occurs at a confining pressure between 35 MPa and 55 MPa, close to the experimental value.

4.2.2 Crack densities

Nicolas *et al.* (2016) inverted elastic wave velocity data to infer axial crack densities (Fig. 16a). Experimental results are compared to model predictions (Fig. 16b). Initial damage in the

model is 0.45, corresponding to an initial crack density of 0.105 (thus an initial axial crack density of approximately 0.035). However, cracks are considered as initially closed and initial crack density is 0. Experimental and predicted crack density evolutions during constant strain rate experiments are reasonably similar (Fig. 16). Below the brittle-ductile transition, the model reproduces the experimental axial crack density values during deformation. Predicted axial crack densities at a given volumetric strain are close to measured ones and remain relatively low (below 0.1).

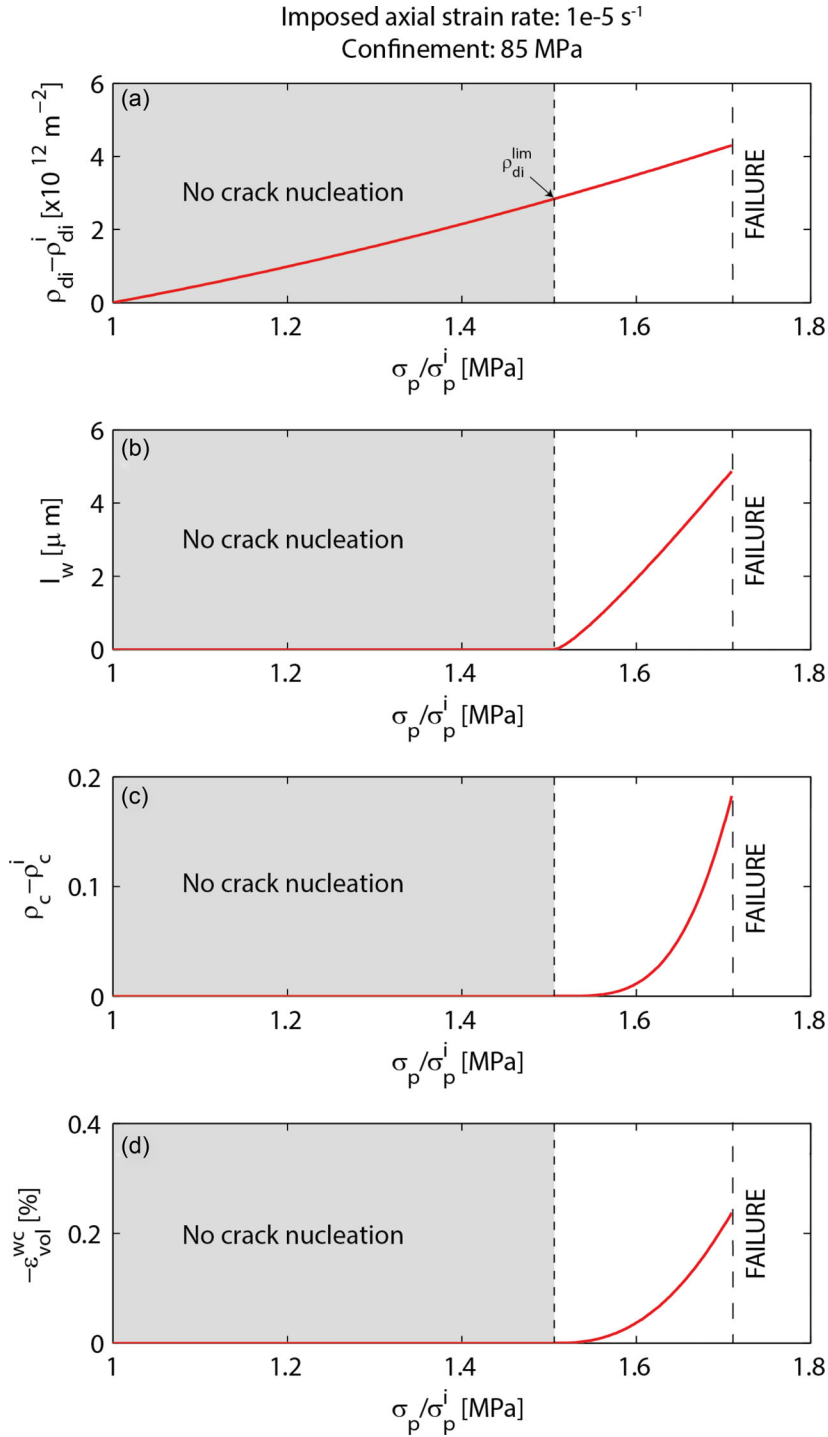


Figure 13. Compilation of mechanical parameters linked to new crack nucleation. (a) Evolution of the strain-induced dislocation density as a function of the reference stress in the plasticity law normalized by its initial value σ_p / σ_p^i . The arrow denotes the onset of new crack nucleation. (b) Evolution of the nucleated crack length as a function of σ_p / σ_p^i . (c) Evolution of the nucleated crack density as a function of σ_p / σ_p^i . (d) Evolution of the volumetric strain due to nucleated cracks as a function of σ_p / σ_p^i .

Above the brittle-ductile transition, the model also reproduces well-enough the experimental axial crack density evolution. Predicted axial crack densities at a given volumetric strain are very close to measured ones. Both experimental and predicted results show a slight increase between the onset on inelastic compaction (C^*) and the post-yield onset of dilatancy ($C^{*'}\prime$) and a dramatic increase beyond $C^{*'}\prime$.

4.3 Limits of the model and possible applications

Initial porosity is a key parameter that controls the deformation and failure modes of limestones (e.g. Vajdova *et al.* 2004). In carbonate rocks, structural heterogeneities can also influence the localization of damage (Dautriat *et al.* 2011a), as well as the microporosity distribution (Regnet *et al.* 2015a). The model takes into account a

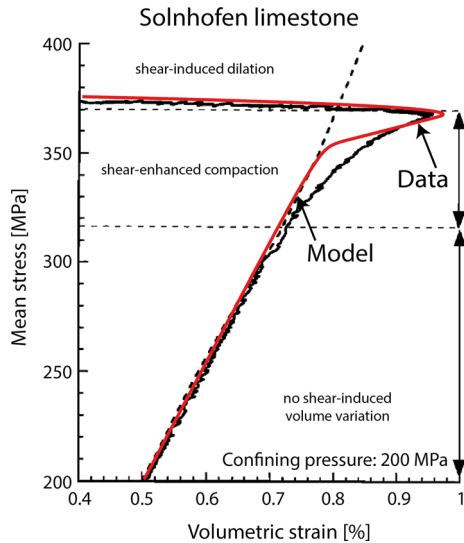


Figure 14. Comparison of the mean stress versus volumetric strain curve predicted by the model developed in this paper with the result of an experiment performed by Baud *et al.* (2000) on Solnhofen limestone at a confining pressure of 200 MPa. Parameters used are reported in Table 3.

dilatancy due to crack development at low confining pressure, and a semi-brittle behaviour characterized by shear-enhanced compaction due to microplastic flow, switching to dilatancy because local stress concentrations caused by pile-ups. To what extent can the model developed here be applied to various carbonate rocks? What is the porosity range of application of the model?

In low porosity limestones, inelastic compaction is the result of plastic pore collapse and grain plasticity (e.g. Fredrich *et al.* 1989; Baud *et al.* 2000). For example, Baud *et al.* (2000) interpreted shear-enhanced compaction in Solnhofen limestone (porosity 3 per cent) as resulting from plastic collapse of spherical pores embedded in a solid matrix, as initially modelled by Curran & Carroll (1979). These mechanisms of deformation are those taken into account in the model, which should therefore predict adequately the mechanical behaviour of low porosity limestones.

Baud *et al.* (2009) investigated systematically the micromechanics of compaction in two high porosity carbonates, Majella grainstone (porosity 30 per cent) and Saint-Maximin limestone (porosity

37 per cent). In Majella grainstone, shear-enhanced compaction is followed by shear failure with the apparition of a compactive shear band at low confining pressure (5–10 MPa), and homogeneous cataclastic flow at higher confining pressure (> 10 MPa). In both cases, grain crushing is the dominant mechanism of deformation beyond C^* . In Saint-Maximin limestone, Baud *et al.* (2009) could not unambiguously determine the evolution of the failure mode with increasing pressure but they observed various patterns of strain localization in all their samples. In a third high porosity limestone, Estailades limestone (porosity: 28 per cent), Dautriat *et al.* (2011b) showed that beyond elastic compaction, cataclastic compaction is coupled with an elastic wave velocity decrease due to grain crushing. It can be concluded that the micromechanisms of deformation in Majella grainstone, Saint-Maximin and Estailades limestones are very different from the micromechanisms taken into account in the model developed in this study. The mechanical behaviour of high porosity limestones (porosity higher than 20 per cent), where grain crushing is the main mechanism of inelastic compaction, cannot be accounted for by the present model. Thus, up to what porosity can the model predict the mechanical behaviour?

For porosities lower than 15 per cent, deformation beyond C^* in the semi-brittle regime and inelastic pore collapse are controlled by plastic micromechanisms (dislocation slip processes, twinning) associated with some microcracking (Vajdova *et al.* 2004). Thus, it can be suggested that, as porosity increases, a transitional behaviour is likely to develop and volumetric strain due to shearing and rotation of fragments (Peng & Johnson 1972; Vajdova *et al.* 2012) becomes more important. The transition between shear-enhanced compaction controlled by crystal plasticity and grain crushing is likely to occur for a porosity of approximately 20 per cent (Vajdova *et al.* 2004) and the present model probably predicts adequately the stress–strain evolution for carbonates of porosity lower than 20 per cent.

Compaction of porous rocks is known to be localized in many cases, as shown in sandstones by Mollema & Antonellini (1996) and Fortin *et al.* (2005) among many others. Baud *et al.* (2009) observed compactive shear bands at low confinement in Majella grainstone and at all confining pressures in Saint-Maximin limestone, suggesting that compaction localization is important in the mechanical compaction of high porosity carbonates. This kind of phenomenon has not been considered here because experimental results do not show localization of compaction for low porosity limestones. The

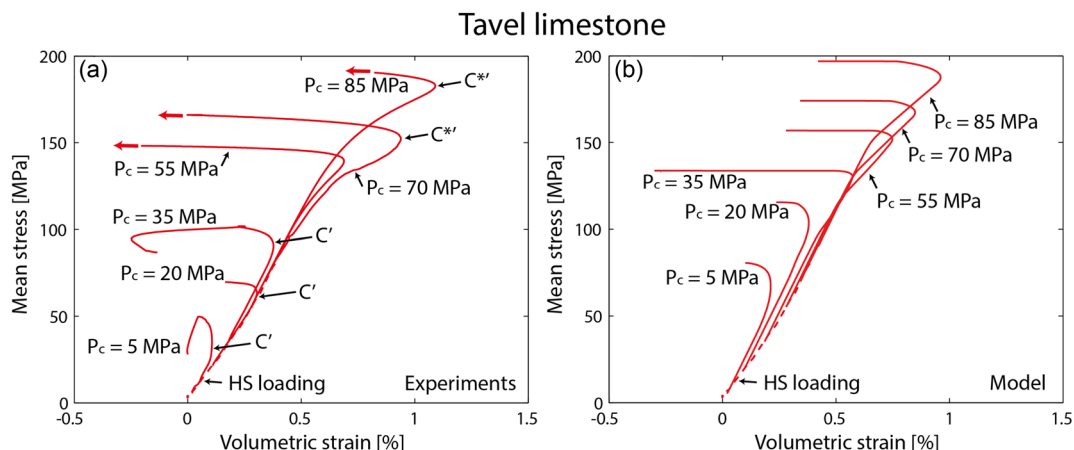


Figure 15. (a) Mean stress as a function of volumetric strain for experiments conducted at confining pressures ranging from 0 to 85 MPa for dry Tavel limestone samples at $T = 70^\circ\text{C}$ (Nicolas *et al.* 2016). The dashed line corresponds to the behaviour under hydrostatic loading and is shown for reference. (b) Corresponding model predictions for various confining pressures, using parameters determined for $P_c = 85$ MPa. The dashed line corresponds to the experimentally obtained behaviour under hydrostatic loading and is shown for reference.

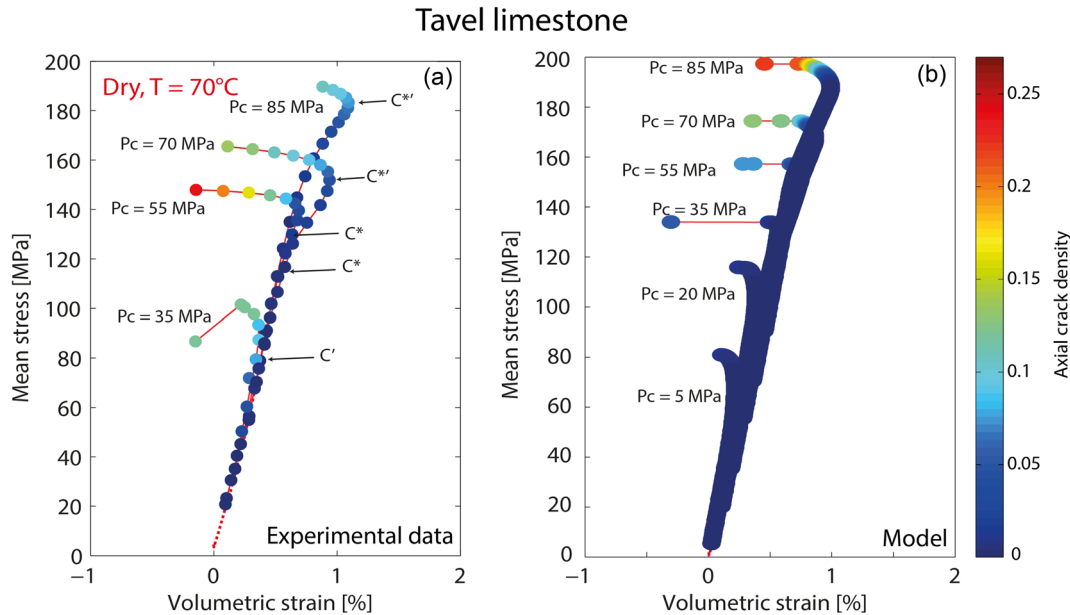


Figure 16. Comparison of the experimental mean stress versus volumetric strain (a) and the model prediction (b) for deformation of Tavel limestone at various confining pressures. The colour of the dots represents the vertical crack density. Initial damage in the model is 0.45, corresponding to an initial crack density of 0.105 (thus an initial axial crack density of approximately 0.035). However, cracks are considered as initially closed and initial crack density is 0.

present model is based on the assumption of homogeneous inelastic compaction and homogeneous development of damage. This kind of approach allows to compute an homogeneous deformation of the medium and can be considered as complementary to a localization deformation approach (i.e. bifurcation theory, see Bésuelle & Rudnicki (2003)). The similarities and differences of these two approaches can be found in Guéguen & Bésuelle (2007).

Compaction is sometimes induced by the production of reservoirs (Fredrich *et al.* 2000). It can cause subsidence (e.g. Morton *et al.* 2006), which requires to redesign offshore platforms, or induce seismicity (e.g. Segall 1989) and well failure (e.g. Bruno *et al.* 1992), among other problems (Nagel 2001). For low porosity (i.e. $\phi < 20$ per cent) limestones, the present model can provide insights into the macroscopic mechanical behaviour of reservoirs. Moreover, as shown by David *et al.* (1994) among others, compaction can lead to changes of permeability that can impact aquifer and reservoir production. As the present model is micromechanically derived and based on damage theory, coupling it with permeability models (e.g. Guéguen & Dienes 1989; Simpson *et al.* 2001; Ghabezloo *et al.* 2009; Perol & Bhat 2016) could provide insights into the joint evolution of damage and permeability of reservoirs (e.g. Brehme *et al.* 2016).

5 CONCLUSIONS

The complex general trends of stress–strain relations of low-porosity limestones is reproduced by a model based on (1) brittle crack propagation, (2) a plasticity law for porous media with hardening and (3) crack nucleation due to dislocation pile-ups. The model is based on (i) three parameters relevant to the brittle behaviour (pre-existing crack length and density, sliding coefficient on these cracks), as previously developed by Ashby & Sammis (1990), (ii) two parameters relevant to the microplastic flow in the solid non-porous medium (a reference strain rate and an initial yield stress), and (iii) a parameter characterising the density of large pile-ups. Parameters relevant to the brittle behaviour can be determined from

observations of the microstructure. The parameters relevant to the ductile behaviour are fitted to experimental data. Note that the three free parameter values related to the semi-brittle behaviour are identified for a given semi-brittle experiment (at the highest confining pressure). Predictions for other confining pressures are using these three identified parameter values.

Despite the limited number of parameters, the model adequately predicts a brittle behaviour at low confining pressures, which switches to a semi-brittle behaviour characterized by inelastic compaction followed by dilatancy at higher confining pressures. This suggests that the microphysical phenomena responsible for the deformation are sufficient well captured. Possible applications include reservoir management. More generally, predicting the complex rheology of porous limestones in various conditions is possible through this model.

ACKNOWLEDGEMENTS

One anonymous reviewer and Erik Rybacki are acknowledged for their very constructive comments that greatly improved the manuscript. AN thanks H.S. Bhat for insightful discussions and comments. AN benefited from stimulating discussions with P. Marchina, T.-F. Wong, Y.M. Leroy, J.B. Regnet, A. Schubnel, P. Baud, C. David, A. Dimanov, B.A. Verberne, O. Plümper, J. De Bresser and C.J. Spiers throughout his PhD. This project was funded by a grant provided by Total No. FR00006158.

REFERENCES

- Adelinet, M., Fortin, J. & Guéguen, Y., 2011. Dispersion of elastic moduli in a porous-cracked rock: theoretical predictions for squirt-flow, *Tectonophysics*, **503**(1), 173–181.
- Anselmetti, F.S. & Eberli, G.P., 1993. Controls on sonic velocity in carbonates, *Pure appl. Geophys.*, **141**(2–4), 287–323.
- Armijo, R. & Lyon-Caen, H.D.P., 1992. East-west extension and holocene normal-fault scarps in the hellenic arc, *Geology*, **20**, 491–494.

- Ashby, M. & Hallam, S., 1986. The failure of brittle solids containing small cracks under compressive stress states, *Acta Metall.*, **34**(3), 497–510.
- Ashby, M. & Sammis, C.G., 1990. The damage mechanics of brittle solids in compression, *Pure appl. Geophys.*, **133**, 489–521.
- Atkinson, B.K., 1984. Subcritical crack growth in geological materials, *J. geophys. Res.*, **89**(B6), 4077–4114.
- Baechle, G.T., Colpaert, A., Eberli, G.P. & Weger, R.J., 2008. Effects of microporosity on sonic velocity in carbonate rocks, *Leading Edge*, **27**(8), 1012–1018.
- Baud, P., Schubnel, A. & Wong, T.-F., 2000. Dilatancy, compaction, and failure mode in Solnhofen limestone, *J. geophys. Res.*, **105**(B8), 19 289–19 303.
- Baud, P., Vinciguerra, S., David, C., Cavallo, A., Walker, E. & Reuschlé, T., 2009. Compaction and failure in high porosity carbonates: mechanical data and microstructural observations, *Pure appl. Geophys.*, **166**, 869–898.
- Bésuelle, P. & Rudnicki, J.W., 2003. Localization: shear bands and compaction bands, *Int. Geophys.*, **89**, 219–321.
- Bhat, H., Sammis, C. & Rosakis, A., 2011. The micromechanics of westerley granite at large compressive loads, *Pure appl. Geophys.*, **168**(12), 2181–2198.
- Bhat, H.S., Rosakis, A.J. & Sammis, C.G., 2012. A micromechanics based constitutive model for brittle failure at high strain rates, *J. Appl. Mech.*, **79**(3), 031016.1–031016.12.
- Brace, W., 1978. Volume changes during fracture and frictional sliding: A review, *Pure appl. Geophys.*, **116**, 603–614.
- Brailon, P. & Serughetti, J., 1976. Mechanical twinning in calcite. observation of twinning dislocations and planar defects by transmission electron microscopy, *Phys. Status Solidi a*, **33**(1), 405–413.
- Brantut, N., 2015. Time-dependent recovery of microcrack damage and seismic wave speeds in deformed limestone, *J. geophys. Res.*, **120**(12), 8088–8109.
- Brantut, N., Heap, M.J., Baud, P. & Meredith, P.G., 2014. Mechanisms of time-dependent deformation in porous limestone, *J. geophys. Res.*, **119**(7), 5444–5463.
- Brehme, M., Blöcher, G., Cacace, M., Kamah, Y., Sauter, M. & Zimmermann, G., 2016. Permeability distribution in the lahendong geothermal field: a blind fault captured by thermal–hydraulic simulation, *Environ. Earth Sci.*, **75**(14), 1–11.
- Bristow, J.R., 1960. Microcracks, and the static and dynamic elastic constants of annealed and heavily cold-worked metals, *Br. J. Appl. Phys.*, **11**(2), 81–85.
- Bruno, M. *et al.*, 1992. Subsidence-induced well failure, *SPE Drill. Eng.*, **7**(2), 148–152.
- Budiansky, B. & O’Connell, R.J., 1976. Elastic moduli of a cracked solid, *Int. J. Solids Struct.*, **12**(2), 81–97.
- Budiansky, B., Hutchinson, J. & Slutsky, S., 1982. *Void Growth and Collapse in Viscous Solids*, Pergamon Press.
- Curran, J.H. & Carroll, M.M., 1979. Shear stress enhancement of void compaction, *J. geophys. Res.*, **84**(B3), 1105–1112.
- Danas, K. & Castañeda, P.P., 2012. Influence of the lode parameter and the stress triaxiality on the failure of elasto-plastic porous materials, *Int. J. Solids Struct.*, **49**(11–12), 1325–1342.
- Dautriat, J., Bornert, M., Gland, N., Dimanov, A. & Raphanel, J., 2011a. Localized deformation induced by heterogeneities in porous carbonate analysed by multi-scale digital image correlation, *Tectonophysics*, **503**(1), 100–116.
- Dautriat, J., Gland, N., Dimanov, A. & Raphanel, J., 2011b. Hydromechanical behavior of heterogeneous carbonate rock under proportional triaxial loadings, *J. geophys. Res.*, **116**, B01205, doi:10.1029/2009jb000830.
- David, C., Wong, T.-F., Zhu, W. & Zhang, J., 1994. Laboratory measurement of compaction-induced permeability change in porous rocks: implications for the generation and maintenance of pore pressure excess in the crust, *Pure appl. Geophys.*, **143**(1), 425–456.
- De Bresser, J., 1996. Steady state dislocation densities in experimentally deformed calcite materials: single crystals versus polycrystals, *J. geophys. Res.*, **101**(B10), 22 189–22 201.
- De Bresser, J. & Spiers, C., 1997. Strength characteristics of the r, f, and c slip systems in calcite, *Tectonophysics*, **272**(1), 1–23.
- Deshpande, V. & Evans, A.G., 2008. Inelastic deformation and energy dissipation in ceramics: A mechanism-based constitutive model, *J. Mech. Phys. Solids*, **56**, 3077–3100.
- Dimanov, A., Rybacki, E., Wirth, R. & Dresen, G., 2007. Creep and strain-dependent microstructures of synthetic anorthite–diopside aggregates, *J. Struct. Geol.*, **29**(6), 1049–1069.
- Duva, J. & Hutchinson, J., 1984. Constitutive potentials for dilutely voided nonlinear materials, *Mech. Mater.*, **3**(1), 41–54.
- Eberli, G.P., Baechle, G.T., Anselmetti, F.S. & Incze, M.L., 2003. Factors controlling elastic properties in carbonate sediments and rocks, *Leading Edge*, **22**(7), 654–660.
- Eshelby, J., Frank, F. & Nabarro, F., 1951. The equilibrium of linear arrays of dislocations., *London Edinburgh Dublin Phil. Mag. J. Sci.*, **42**(327), 351–364.
- Evans, A., Meyer, M., Fertig, K., Davis, B. & Baumgartner, H., 1980. Probabilistic models for defect initiated fracture in ceramics, *J. Nondestruct. Eval.*, **1**(2), 111–122.
- Evans, B., Fredrich, J.T. & Wong, T.-F., 1990. The brittle-ductile transition in rocks: recent experimental and theoretical progress, in *The Brittle-Ductile Transition in Rocks*, pp. 1–20, eds Duba, A. G., Durham, W. B., Handin, J. W. & Wang, H. F., American Geophysical Union.
- Fortin, J., Schubnel, A. & Guéguen, Y., 2005. Elastic wave velocities and permeability evolution during compaction of Bleurswiler sandstone, *Int. J. Rock Mech. Min. Sci.*, **42**(7), 873–889.
- Fortin, J., Guéguen, Y. & Schubnel, A., 2007. Effects of pore collapse and grain crushing on ultrasonic velocities and Vp/Vs, *J. geophys. Res.*, **112**, B08207, doi:10.1029/2005JB004005.
- Fortin, J., Pimienta, L., Guéguen, Y., Schubnel, A., David, E. & Adelinet, M., 2014. Experimental results on the combined effects of frequency and pressure on the dispersion of elastic waves in porous rocks, *Leading Edge*, **33**(6), 648–654.
- Fredrich, J.T., Evans, B. & Wong, T.-F., 1989. Micromechanics of the brittle to plastic transition in Carrara marble, *J. geophys. Res.*, **94**(B4), 4129–4145.
- Fredrich, J.T., Evans, B. & Wong, T.-F., 1990. Effect of grain size on brittle and semibrittle strength: Implications for micromechanical modelling of failure in compression, *J. geophys. Res.*, **95**(B7), 10 907–10 920.
- Fredrich, J.T., Arguello, J.G., Deitrick, G.L. & de Rouffignac, E.P., 2000. Geomechanical modeling of reservoir compaction, surface subsidence, and casing damage at the Belridge diatomite field, *SPE Reservoir Eval. Eng.*, **3**, 348–359.
- Ghabezloo, S., Sulem, J., Guédon, S. & Martineau, F., 2009. Effective stress law for the permeability of a limestone, *Int. J. Rock Mech. Min. Sci.*, **46**(2), 297–306.
- Gilman, J.J., 1960. Direct measurements of the surface energies of crystals, *J. Appl. Phys.*, **31**(12), 2208–2218.
- Goldscheider, N., Mádl-Szőnyi, J., Eröss, A. & Schill, E., 2010. Review: thermal water resources in carbonate rock aquifers, *Hydrogeol. J.*, **18**(6), 1303–1318.
- Griggs, D.T., Turner, F.J. & Heard, H.C., 1960. Chapter 4: Deformation of rocks at 500° to 800 °C, *Geol. Soc. Am. Mem.*, **79**, 39–104.
- Guéguen, Y. & Bésuelle, P., 2007. Damage and localization: two key concepts in rock deformation studies, *Geol. Soc., London, Spec. Publ.*, **289**(1), 7–17.
- Guéguen, Y. & Dienes, J., 1989. Transport properties of rocks from statistics and percolation, *Math. Geol.*, **21**(1), 1–13.
- Guéguen, Y. & Kachanov, M., 2011. Effective elastic properties of cracked rocks - an overview, in *Mechanics of crustal rocks, CISM Courses and Lectures*, **533**, 73–125.
- Guéguen, Y., Sarout, J., Fortin, J. & Schubnel, A., 2009. Cracks in porous rocks: tiny defects, strong effects, *Leading Edge*, **28**(1), 40–47.
- Heap, M., Mollo, S., Vinciguerra, S., Lavallée, Y., Hess, K.-U., Dingwell, D., Baud, P. & Iezzi, G., 2013. Thermal weakening of the carbonate basement under Mt. Etna volcano (Italy): implications for volcano instability, *J. Volcanol. Geotherm. Res.*, **250**(0), 42–60.

- Heard, H.C., 1960. Chapter 7: Transition from brittle fracture to ductile flow in Solenhofen limestone as a function of temperature, confining pressure, and interstitial fluid pressure, *Geol. Soc. Am. Mem.*, **79**, 193–226.
- Heard, H. & Raleigh, C., 1972. Steady-state flow in marble at 500 to 800 °C, *Bull. geol. Soc. Am.*, **83**(4), 935–956.
- Hirth, J.P. & Lothe, J., 1982. *Theory of Dislocations*, Krieger Publishing Company.
- Homand, F. et al., 2000. *Manuel de mécanique des roches* (Tome 1, Fondements), Presses des MINES.
- Kachanov, M., 1993. Elastic solids with many cracks and related problems, *Adv. Appl. Mech.*, **30**, 259–445.
- Kachanov, M. & Sevostianov, I., 2012. Rice's internal variables formalism and its implications for the elastic and conductive properties of cracked materials, and for the attempts to relate strength to stiffness, *J. Appl. Mech.*, **79**(3), 031002, doi:10.1115/1.4005957.
- Karato, S.-i., 2008. *Deformation of Earth Materials: An Introduction to the Rheology of Solid Earth*, Cambridge Univ. Press.
- Kassner, M., 2004. Taylor hardening in five-power-law creep of metals and Class M alloys, *Acta Mater.*, **52**(1), 1–9.
- Keith, R. & Gilman, J., 1960. Dislocation etch pits and plastic deformation in calcite, *Acta Metall.*, **8**(1), 1–10.
- Kirby, S.H. & Raleigh, C., 1973. Mechanisms of high-temperature, solid-state flow in minerals and ceramics and their bearing on the creep behavior of the mantle, *Tectonophysics*, **19**(2), 165–194.
- Kohlstedt, D., Evans, B. & Mackwell, S. et al. 1995. Strength of the lithosphere: constraints imposed by laboratory experiments, *J. geophys. Res.*, **100**, 17–587.
- Lucia, F.J., 2007. *Carbonate Reservoir Characterization: An Integrated Approach*, Springer Science & Business Media.
- Mackenzie, J.K., 1950. The elastic constants of a solid containing spherical holes, *Proc. Phys. Soc. B*, **63**(1), 2–11.
- Mallet, C., Fortin, J., Guéguen, Y. & Bouyer, F., 2013. Effective elastic properties of cracked solids: an experimental investigation, *Int. J. Fract.*, **182**(2), 275–282.
- Mallet, C., Fortin, J., Guéguen, Y. & Bouyer, F., 2015. Brittle creep and subcritical crack propagation in glass submitted to triaxial conditions, *J. geophys. Res.*, **120**(2), 879–893.
- Meyers, M.A., Armstrong, R.W. & Kirchner, H.O., 1999. *Mechanics and Materials: Fundamentals and Linkages*, Wiley-VCH.
- Miguel, M.-C., Vespignani, A., Zapperi, S., Weiss, J. & Grasso, J.-R., 2001. Intermittent dislocation flow in viscoplastic deformation, *Nature*, **410**(6829), 667–671.
- Mollema, P. & Antonellini, M., 1996. Compaction bands: a structural analog for anti-mode I cracks in aeolian sandstone, *Tectonophysics*, **267**(1), 209–228.
- Morton, R.A., Bernier, J.C. & Barras, J.A., 2006. Evidence of regional subsidence and associated interior wetland loss induced by hydrocarbon production, Gulf Coast region, USA, *Environ. Geol.*, **50**(2), 261–274.
- Mouslopoulou, V., Moraetis, D., Benedetti, L., Guillou, V., Bellier, O. & Hristopoulos, D., 2014. Normal faulting in the forearc of the Hellenic subduction margin: Paleoearthquake history and kinematics of the Spili Fault, Crete, Greece, *J. Struct. Geol.*, **66**(0), 298–308.
- Nagel, N., 2001. Compaction and subsidence issues within the petroleum industry: from Wilmington to Ekofisk and beyond, *Phys. Chem. Earth A*, **26**, 3–14.
- Nemat-Nasser, S. & Horii, H., 1982. Compression-induced nonplanar crack extension with application to splitting, exfoliation, and rockburst, *J. geophys. Res.*, **87**(B8), 6805–6821.
- Nicolas, A., Fortin, J., Regnet, J., Dimanov, A. & Guéguen, Y., 2016. Brittle and semi-brittle behaviours of a carbonate rock: influence of water and temperature, *Geophys. J. Int.*, **206**(1), 438–456.
- Nicolas, A., Fortin, J., Regnet, J., Verberne, B., Plümper, O., Dimanov, A., Spiers, C. & Guéguen, Y., 2017. Brittle and semi-brittle creep of tavel limestone deformed at room temperature, *J. geophys. Res.*, **122**(6), 4436–4459.
- Olsson, W.A., 1974. Microfracturing and faulting in a limestone, *Tectonophysics*, **24**(3), 277–285.
- Olsson, W.A. & Peng, S.S., 1976. Microcrack nucleation in marble, *Int. J. Rock Mech. Min. Sci.*, **13**(2), 53–59.
- Orowan, E., 1954. *Dislocations in Metals*, AIME, p. 131.
- Paterson, M., 1978. *Experimental Rock Deformation: The Brittle Field*, Springer-Verlag.
- Paterson, M.S. & Wong, T.-F., 2005. *Experimental Rock Deformation - The Brittle Field*, Springer-Verlag.
- Peng, S. & Johnson, A., 1972. Crack growth and faulting in cylindrical specimens of Chelmsford granite, *Int. J. Rock Mech. Min. Sci. Geomech. Abstr.*, **9**(1), 37–86.
- Perol, T. & Bhat, H.S., 2016. Micromechanics-based permeability evolution in brittle materials at high strain rates, *Pure appl. Geophys.*, **173**(8), 2857–2868.
- Pimienta, L., Fortin, J. & Guéguen, Y., 2015. Bulk modulus dispersion and attenuation in sandstones, *Geophysics*, **80**(2), D111–D127.
- Poirier, J.-P., 1985. *Creep of Crystals: High-temperature Deformation Processes in Metals, Ceramics and Minerals*, Cambridge Univ. Press.
- Regnet, J.B., David, C., Fortin, J., Robion, P., Makhloufi, Y. & Collin, P., 2015a. Influence of microporosity distribution on the mechanical behaviour of oolitic carbonate rocks, *Geomech. Energy Environ.*, **3**, 11–23.
- Regnet, J.B., Robion, P., David, C., Fortin, J., Brigaud, B. & Yven, B., 2015b. Acoustic and reservoir properties of microporous carbonate rocks: Implication of micrite particle size and morphology, *J. geophys. Res.*, **120**(2), 790–811.
- Renner, J. & Evans, B., 2002. Do calcite rocks obey the power-law creep equation?, *Geol. Soc., London, Spec. Publ.*, **200**(1), 293–307.
- Renner, J., Evans, B. & Siddiqi, G., 2002. Dislocation creep of calcite, *J. geophys. Res.*, **107**(B12), 2364, doi:10.1029/2001JB001680.
- Rhett, D.W. & Farrell, H.E., 1991. Effect of reservoir depletion and pore pressure drawdown on in situ stress and deformation in the Ekofisk field, North Sea, in *The 32nd US Symposium on Rock Mechanics (USRMS)*, 10–12 July, Norman, Oklahoma.
- Rice, J. & Tracey, D., 1969. On the ductile enlargement of voids in triaxial stress fields, *J. Mech. Phys. Solids*, **17**(3), 201–217.
- Risnes, R., Madland, M., Hole, M. & Kwabiah, N., 2005. Water weakening of chalk-mechanical effects of water-glycol mixtures, *J. Pet. Sci. Eng.*, **48**(1), 21–36.
- Ross, J.V. & Lewis, P.D., 1989. Brittle-ductile transition: Semi-brittle behaviour, *Tectonophysics*, **167**(1), 75–79.
- Royne, A., Bisschop, J. & Dysthe, D.K., 2011. Experimental investigation of surface energy and subcritical crack growth in calcite, *J. geophys. Res.*, **116**, B04204, doi:10.1029/2010JB008033.
- Rutter, E., 1974. Influence of temperature, strain rate and interstitial water in experimental deformation of calcite rocks, *Tectonophysics*, **22**, 311–334.
- Rutter, E., 1986. On the nomenclature of mode of failure transitions in rocks, *Tectonophysics*, **122**(3–4), 381–387.
- Rybacki, E., Evans, B., Janssen, C., Wirth, R. & Dresen, G., 2013. Influence of stress, temperature, and strain on calcite twins constrained by deformation experiments, *Tectonophysics*, **601**, 20–36.
- Sayers, C.M. & Kachanov, M., 1995. Microcrack-induced elastic wave anisotropy of brittle rocks, *J. geophys. Res.*, **100**(B3), 4149–4156.
- Schmid, S., Boland, J. & Paterson, M., 1977. Superplastic flow in finegrained limestone, *Tectonophysics*, **43**(3–4), 257–291.
- Schubnel, A., Walker, E., Thompson, B.D., Fortin, J., Guéguen, Y. & Young, R.P., 2006. Transient creep, aseismic damage and slow failure in Carrara marble deformed across the brittle-ductile transition, *Geophys. Res. Lett.*, **33**, L17301, doi:10.1029/2006GL026619.
- Segall, P., 1989. Earthquakes triggered by fluid extraction, *Geology*, **17**(10), 942–946.
- Shapiro, B. & Kachanov, M., 1997. Materials with fluid-filled pores of various shapes: Effective elastic properties and fluid pressure polarization, *Int. J. Solids Struct.*, **34**(27), 3517–3540.
- Simpson, G., Guéguen, Y. & Schneider, F., 2001. Permeability enhancement due to microcrack dilatancy in the damage regime, *J. geophys. Res.*, **106**(B3), 3999–4016.
- Smith, E. & Barnby, J., 1967. Crack nucleation in crystalline solids, *Met. Sci.*, **1**(1), 56–64.

- Startsev, V., Bengus, V., Lavrent'ev, F. & Soifer, L., 1960. Formation of dislocations in the twinning of calcite, *Kristallografiya*, **5**(5), 737–741.
- Stocker, R. & Ashby, M., 1973. On the rheology of the upper mantle, *Rev. Geophys.*, **11**(2), 391–426.
- Stroh, A., 1954. The formation of cracks as a result of plastic flow, *Proc. R. Soc. A*, **223**(1154), 404–414.
- Stroh, A.N., 1957. A theory of the fracture of metals, *Adv. Phys.*, **6**(24), 418–465.
- Tada, H., Paris, P.C. & Irwin, G.R., 2000. *The Stress Analysis of Cracks Handbook*, The American Society of Mechanical Engineers.
- Taylor, G.I., 1934. The mechanism of plastic deformation of crystals. Part I. Theoretical, *Proc. R. Soc. A*, **145**, 362–387.
- Turner, F.J., Griggs, D.T. & Heard, H., 1954. Experimental deformation of calcite crystals, *Bull. geol. Soc. Am.*, **65**(9), 883–934.
- Vajdova, V., Baud, P. & Wong, T.-F., 2004. Compaction, dilatancy, and failure in porous carbonate rocks, *J. geophys. Res.*, **109**, B05204, doi:10.1029/2003JB002508.
- Vajdova, V., Zhu, W., Chen, T.-M.N. & Wong, T.-F., 2010. Micromechanics of brittle faulting and cataclastic flow in Tavel limestone, *J. Struct. Geol.*, **32**(8), 1158–1169.
- Vajdova, V., Baud, P., Wu, L. & fong Wong, T., 2012. Micromechanics of inelastic compaction in two allochemical limestones, *J. Struct. Geol.*, **43**(0), 100–117.
- Vincké, O., Boutéca, M. & Piau, J., 1998. Study of the effective stress at failure, in *Poromechanics, a Tribute to Maurice A. Biot*, pp. 635–639, ed. Balkema, A.A., Rotterdam.
- Walsh, J., 1965a. The effect of cracks on the uniaxial elastic compression of rocks, *J. geophys. Res.*, **70**(2), 399–411.
- Walsh, J.B., 1965b. The effect of cracks on the compressibility of rock, *J. geophys. Res.*, **70**(2), 381–389.
- Wang, Z.-C., Bai, Q., Dresen, G., Wirth, R. & Evans, B., 1996. High-temperature deformation of calcite single crystals, *J. geophys. Res.*, **101**(B9), 20 377–20 390.
- Weertman, J., 1975. High temperature creep produced by dislocation motion, in *Rate Processes in Plastic Deformation of Materials*, pp. 315–336 eds Li, J.C.M. & Mukherjee, A.K., ASM.
- Willemse, E.J., Peacock, D.C. & Aydin, A., 1997. Nucleation and growth of strike-slip faults in limestones from Somerset, UK, *J. Struct. Geol.*, **19**(12), 1461–1477.
- Wong, T.-F., 1990. A note on the propagation behavior of a crack nucleated by a dislocation pileup, *J. geophys. Res.*, **95**(B6), 8639–8646.
- Wong, T.-F. & Baud, P., 2012. The brittle-ductile transition in porous rock: a review, *J. Struct. Geol.*, **44**(0), 25–53.
- Wong, T.-F., David, C. & Zhu, W., 1997. The transition from brittle faulting to cataclastic flow in porous sandstones: mechanical deformation, *J. geophys. Res.*, **102**(B2), 3009–3025.
- Xiao, X. & Evans, B., 2003. Shear-enhanced compaction during non-linear viscous creep of porous calcite–quartz aggregates, *Earth planet. Sci. Lett.*, **216**(4), 725–740.
- Zhu, W., Baud, P. & Wong, T.-F., 2010. Micromechanics of cataclastic pore collapse in limestone, *J. geophys. Res.*, **115**, B04405, doi:10.1029/2009JB006610.

APPENDIX A: DERIVATION OF THE INITIAL ELASTIC MODULI OF THE CRACKED POROUS ROCK

Section 2.1 describes the evolution of the elastic moduli during deformation of the rock, based on the initial elastic moduli of the cracked porous medium. If the initial moduli are unknown, they can be calculated as a function of the initial crack density (ρ_c^i) and porosity (p). Following Fortin *et al.* (2007), in the dry case, for an isotropic distribution of cracks orientations, the initial shear modulus G_i and bulk modulus K_i

of a medium containing spheroidal pores and cracks can be expressed as:

$$\frac{G_0}{G_i} = 1 + \frac{\rho_c^i}{1-p} \frac{h}{1+\nu_0} \left(1 - \frac{\nu_0}{5}\right) + \frac{p}{1-p} \frac{15(1-\nu_0)}{7-5\nu_0}, \quad (\text{A1})$$

$$\frac{K_0}{K_i} = 1 + \frac{\rho_c^i}{1-p} \frac{h}{1-2\nu_0} \left(1 - \frac{\nu_0}{2}\right) + \frac{p}{1-p} \frac{3(1-\nu_0)}{1-2\nu_0}, \quad (\text{A2})$$

where G_0 and K_0 are the shear and bulk moduli of the crack- and porosity-free matrix, and ν_0 is the Poisson coefficient of the matrix. The factor h describes the penny-shaped geometry and is given in the main text (eq. 3). Once the initial moduli are calculated, eq. (2) can be used to compute their evolution with deformation. Note that eq. (2) comes from the fact that G_0/G_i and K_0/K_i are linear with respect to ρ_c for constant p .

Elastic moduli of the crack-free porous medium are needed to calculate strain energy density due to crack propagation (Section 2.2). These crack-free porous medium moduli (G_u , K_u) can be calculated as a function of G_0 , K_0 and p with eqs (A1) and (A2), simply considering that $\rho_c = 0$.

APPENDIX B: CONSTANTS USED TO CALCULATE MACROSCOPIC STRAINS RELATED TO CRACK GROWTH

In this appendix, the reader can find the expressions of the constants used to calculate the macroscopic strains related to crack growth (Section 2.2). The derivation of these constants can be found in Deshpande & Evans (2008). The constants related to the generalization to arbitrary stress states of the growth of wing cracks from pre-existing flaws are (Deshpande & Evans 2008):

$$A = c_1(c_2A_3 - c_2A_1 + c_3), \quad (\text{B1})$$

$$B = \frac{c_1}{\sqrt{3}}(c_2A_3 + c_2A_1 + c_3), \quad (\text{B2})$$

$$C = A + \gamma \sqrt{\alpha \left(\frac{D}{D_0}\right)^{1/3}}, \quad (\text{B3})$$

$$F^2 = \frac{B^2C^2}{C^2 - A^2}, \quad (\text{B4})$$

where $\alpha = \cos \psi$, D_0 and D are the initial and current damage, respectively, and:

$$c_1 = \frac{1}{\pi^2 \alpha^3 [(D/D_0)^{1/3} - 1 + (\beta/\alpha)]^{3/2}},$$

$$c_2 = 1 + 2 \left[\left(\frac{D}{D_0} \right)^{1/3} - 1 \right]^2 \left(\frac{D_0^{2/3}}{1 - D^{2/3}} \right),$$

$$c_3 = 2\alpha^2 \pi^2 \left[\left(\frac{D}{D_0} \right)^{1/3} - 1 \right]^2,$$

$$A_1 = \pi \sqrt{\frac{\beta}{3}} [\sqrt{1 + \mu^2} - \mu],$$

$$A_3 = A_1 \left[\frac{\sqrt{1 + \mu^2} + \mu}{\sqrt{1 + \mu^2} - \mu} \right], \quad (\text{B5})$$

where μ is the Coulomb friction coefficient on the sliding faces of the initial crack and β is a constant found to be equal to $\beta = 0.27$ for 2-D and 3-D cases (Ashby & Sammis 1990). The values given to the parameters relevant to crack propagation can be found in Section 3.2.

APPENDIX C: FROM DISLOCATION SLIP TO A PLASTICITY LAW

The plastic strain-rate $\dot{\varepsilon}^p$ induced by dislocation slip (assuming all dislocations to be mobile) is (Orowan 1954):

$$\dot{\varepsilon}^p = \dot{\varepsilon}^d = \rho_d b v, \quad (C1)$$

where ρ_d is the dislocation density, b is their Burger vector and v their average slip velocity. This approach is valid for stationary average microstructures with mobile dislocations. At low temperature in calcite, dislocations are blocked at obstacles such as grain boundaries and local defects, implying that (1) ρ_d is not constant and (2) dislocations are not all mobile. Furthermore, (3) dislocation slip motions are confined on specific planes. To deal with these complexities, let us separate dislocations into mobile and immobile ones: $\rho_d = \rho_{md} + \rho_{id}$, where ρ_{md} and ρ_{id} are mobile and immobile dislocation densities, respectively. Mobile dislocations are responsible for the deformation whereas immobile ones are trapped and are assumed to contribute for a negligible strain. Thus, ρ_d is replaced by ρ_{md} in eq. (C1). Under the assumption that dislocation slip motions are isotropic because of the random grain orientation, the microplastic flow due to mobile dislocations is approximately:

$$\dot{\varepsilon}^{md} = \rho_{md} b v, \quad (C2)$$

Although interactions of dislocations can lead to complex patterns (e.g. Miguel *et al.* 2001), at low temperature, the mean dislocation velocity is assumed to follow a power law stress-dependence (Meyers *et al.* 1999):

$$v = V_0 \left(\frac{\sigma}{\sigma_0} \right)^m, \quad (C3)$$

where V_0 is a temperature-dependent parameter, σ is applied stress, and σ_0 is the stress at which $v = V_0$. Combining eqs (C2) and (C3), one gets:

$$\dot{\varepsilon}^{md} = \rho_{md} b V_0 \left(\frac{\sigma}{\sigma_0} \right)^n = (\rho_d - \rho_{id}) b V_0 \left(\frac{\sigma}{\sigma_0} \right)^n. \quad (C4)$$

The amplitude of any stress component induced by a dislocation at a distance r is $\sigma = Gb/(2\pi r)$, (Hirth & Lothe 1982) and the total dislocation density is $\rho_d = 1/h^2$, where h is the mean spacing between dislocations. Thus, the average internal stress amplitude is:

$$\sigma = \frac{Gb}{2\pi} \rho_d^{1/2} = \frac{Gb}{2\pi} (\rho_{id} + \rho_{md})^{1/2}. \quad (C5)$$

Using eq. (C2), ρ_{md} can be calculated from the microplastic strain rate. Let us separate immobile dislocations into initially present ones and newly nucleated ones: $\rho_{id} = \rho_{id}^{\text{init}} + \rho_{id}^{\text{new}}$. Mobile dislocations are assumed to be trapped when they cross another dislocation. The probability for a dislocation to be trapped can thus be assumed to be proportional to the mobile dislocation density and to their velocity. We define a characteristic time constant for dislocation movements as:

$$\tau_d = \frac{L_g}{v}, \quad (C6)$$

where L_g is the grain size. Using this characteristic time, the increase rate of immobile dislocations is approximated as:

$$\frac{d\rho_{id}}{dt} = \frac{\rho_{md}}{\tau_d} = \frac{\dot{\varepsilon}^{md}}{bL_g}. \quad (C7)$$

Integrating eq. (C7) over time, one gets $\rho_{id}^{\text{new}} = \dot{\varepsilon}^{md}/(bL_g)$, and finally:

$$\rho_{id} = \rho_{id}^{\text{init}} + \frac{\dot{\varepsilon}^{md}}{bL_g}. \quad (C8)$$

Combining eqs (C4), (C5), and (C8), one gets:

$$\dot{\varepsilon}^{md} = \left[\left(\frac{2\pi}{Gb} \right)^2 \sigma^2 - \left(\rho_{id}^{\text{init}} + \frac{\dot{\varepsilon}^{md}}{bL_g} \right) \right] b V_0 \left(\frac{\sigma}{\sigma_0} \right)^n. \quad (C9)$$

Defining the following constants:

$$\begin{aligned} A_p &= \left(\frac{2\pi}{Gb} \right)^2; \\ B_p &= \rho_{id}^{\text{new}}; \\ C_p &= \frac{1}{bL_g}; \\ D_p &= b V_0 \left(\frac{1}{\sigma_0} \right)^n, \end{aligned} \quad (C10)$$

we get the following polynomial expression for the plastic strain rate:

$$\dot{\varepsilon}^{md} = [A_p \sigma^2 - B_p - C_p \dot{\varepsilon}^{md}] D_p \sigma^n, \quad (C11)$$

in which hardening is introduced through $C_p \dot{\varepsilon}^{md}$. However, the assumptions made for the development of the micromodel have led to introduce four constants (eqs C10), out of which only two are known (A_p and C_p). The physical law (eq. C11) is different from the empirical law (eq. 10) but describes a similar hardening, as discussed below. The empirical law (eq. 10) is used in the study because it limits the number of free parameters.

Hardening is produced by an increase of the internal stress, resulting from dislocation density increase. Let us compare the hardening law (eq. 11) with the evolution of internal stress. Local stresses due to pile-ups are not considered at this point. Using eqs (C2), (C5), and (C8), it leads to the following internal stress evolution:

$$\sigma_i = \frac{Gb}{2\pi} \left[\rho_{id}^{\text{init}} + \frac{\dot{\varepsilon}^{md}}{bv} + \frac{\dot{\varepsilon}^{md}}{bL_g} \right]^{1/2}. \quad (C12)$$

All the parameters are described in Table 1. We find experimental results presented in Taylor (1934) for stress-strain relation in single crystals if we assume a negligible ρ_{id} and $\dot{\varepsilon}^{md} = C^{st}$. Assuming a significant immobile dislocation density, eq. (C12) is similar to that derived in Kassner (2004) for a stationary regime (constant $\dot{\varepsilon}^{md}$). For polycrystals of calcite, De Bresser (1996) showed that experimental results are in agreement with this relation for mean stresses above 40 MPa, which is the case here.

From eq. (C12), defining $\sigma_i^i = [Gb(\rho_{id}^{\text{init}})^{1/2}]/(2\pi)$, $\dot{\varepsilon}_0 = bv\rho_{id}^{\text{init}}$ and $\varepsilon_0 = bL_g\rho_{id}^{\text{init}}$, one gets the macroscopic internal stress hardening law:

$$\sigma_i = \sigma_i^i \left[1 + \frac{\dot{\varepsilon}^p}{\dot{\varepsilon}_0} + \frac{\varepsilon^p}{\varepsilon_0} \right]^{1/2}. \quad (C13)$$

Using eqs (C2) and (C13), one gets:

$$\frac{\dot{\varepsilon}^p / \dot{\varepsilon}_0}{\varepsilon^p / \varepsilon_0} = \frac{b \rho_{md} L_g}{\varepsilon^p}. \quad (\text{C14})$$

Using $b = 10^{-10} \text{ m}$, $\varepsilon^p = 10^{-2}$, $\rho_{md} = 10^{-12} \text{ m}^{-2}$ (see Figure 13), and $L_g = 10^{-6} \text{ m}$, one gets $(\dot{\varepsilon}^p / \dot{\varepsilon}_0) / (\varepsilon^p / \varepsilon_0) = 10^{-2}$, and $\dot{\varepsilon}^p / \dot{\varepsilon}_0$ can be neglected with respect to $\varepsilon^p / \varepsilon_0$. Thus, the sec-

ond term of eq. (C13) has been neglected, which seems acceptable for low strain rates and is in good agreement with experimental results from Kassner (2004). Eq. (C13) becomes similar to the strain hardening power law (eq. 11), with a strain hardening exponent $M = 1/2$. Note that this microderived internal stress law could be modified in order to take into account temperature effects.